University of Bremen

Alfred Wegener Institute - Helmholtz Centre for Polar and Marine Research

MASTER THESIS

Climate Variability of Coupled and Partially Coupled Numerical Experiments:

a study based on AWI-ESM

Author:
Richard Adesuyan

Matriculation Number:
3130857

First Supervisor:
Prof. Dr. Gerrit Lohmann

Second Supervisor:
Prof. Rüdiger Gerdes

Tutor:
Lars Ackermann

March 2022

Declaration of copyright

Hereby I declare that my Master's Thesis was written without external support and that I did not use any other sources and auxiliary means than those quoted. All statements which are literally or analogously taken from other publications have been identified as quotations and citations.

Declaration with regard to publishing thesis

I agree that for research purposes third parties can use my thesis stored in the University archive.

Bremen / March 2022 **Richard Adesuyan**

Abstract

The variability of the climate system is majorly impacted by the air-sea interaction. Climate model simulations for the past, present, and future provide an estimate of climate variability and climate change. This study investigates the response of the Ocean to the wind stress engendered changes in the North Atlantic region. Feedback in the complex climate system is however not fully explored yet. Partially coupled experiments with fixed wind stress provide an excellent test of wind-stress feedback in the climate system. The focus is on the behavior of the variability using a partial coupling method to constrain the Ocean with prescribed wind forcing in an otherwise fully coupled Earth system model. This enables the assessment of the direct oceanic and the indirect atmospheric response to idealized forced scenarios of prescribed winds over the North Atlantic region.

A partially coupled model as used in this study is a model in which the Ocean and Sea-Ice component has been forced by prescribed wind stress which drives the said component with inherent climatological wind field as the fully coupled model.

While I discuss major climate variability mechanisms, we focus on four principal modes of climate variability related to the dynamics of Earth's Oceans as they react to wind stress forcing: the El Niño–Southern Oscillation (ENSO), North Atlantic Oscillation (NAO), Atlantic Multidecadal Oscillation (AMO) and Atlantic Meridional Overturning Circulation (AMOC). These Principal oscillation modes are of broad interest and considerable importance in understanding the climate trend and dynamics. These variability mechanisms are examined using the partially coupled climate model with the fully coupled model as the reference source.

The results show that there is negative feedback from the Ocean as the interactive wind stress dampens the examined variability indices. Also, the Sea Surface

temperature increases Southward and decreases Northward in the partially coupled simulations (the reverse is the case for the fully coupled simulations) as a link between wind stress and heat transport is established.

Keywords: climate variability; El Niño-Southern Oscillation (Niño 3.4); North Atlantic Oscillation (NAO); Atlantic Multidecadal Oscillation (AMO); Atlantic Meridional Overturning Circulation (AMOC); Sea Surface Temperature (SST).

Contents

Chapter 1

Introduction

We are currently in a warming climate. What will unfold in the future climate can largely be linked to the past as well as the present. The Sea surface temperature (SST) plays a major role in the climate variability as climate change causes an increasingly warmer baseline in SST thus leading to major modes of climate variability deviation (Lim et al., 2018). The SST is largely affected by heat fluxes which also depend on atmospheric wind speed, surface pressure, as well as the temperature difference between the Ocean and atmospheric components and surface Ocean mixing Bjerknes (1964) and Cayan (1992). The effects of the SST change on the atmosphere are difficult to diagnose, particularly across cooler ocean surfaces in the extratropics due to strong internal variability (Xie, 2004). A negative correlation exists between SST and wind speed for large-scale anomalies Okumura et al., (2001) and Mantua et al., (1997) but positive on smaller scales whereas, the wind speed is slower overlying colder SST, it is faster overlying warmer SST, especially observable in the Kuroshio Extension, Gulf Stream, Agulhas Return Current, and the Southern Ocean Small et al., (2008); Vecchi et al., (2004). The prescribed wind stress communicate an anomalous momentum transfer to the Ocean, which when perturbed, can affect the sea ice cover which invariably would have significant implications on the SST especially when the sea ice melt as a result of heat loss (Kovács et al., 2020). These anomalous heat fluxes affect the stability of the atmospheric marine boundary layers resulting in changes in sea level pressure (Kovács et al., 2020).

Understanding the effect of the wind on the past and present climate is, therefore, paramount to forecast its effect on the future climate. However, observational wind data are limited based on the captured duration, for example, National Centers for Environmental Prediction, Climate Forecast System Reanalysis (NCEPcsfr) (Saha et al., 2010) and ERA-Interim reanalysis (ERAI) (Dee et al., 2011). Both data products are from 1980 onward. Assimilating observational wind data into Earth System Model (ESM) is a method of improving the initialization of the fully coupled model (Thoma et al., 2015). It forces the ESM and, in particular, the components with a longer memory like the Ocean close to the observed climate, which is fundamental for any prediction skill. Various techniques and methodologies for Ocean initialization are possible. They can differ by the variables that are used (sea surface temperature (SST), sea surface salinity (SSS), or surface stress), the initialization procedures depth range (Ocean surface or at depth), and whether anomalies or full fields are used. Servonnat et al. (2015) provide a short introduction and summary of several applied methods. In this study, we describe results of the response of the Ocean from a partial coupling technique applied to the Alfred Wegener Institute Earth System Model (AWI-ESM) in which the Ocean and sea-ice component of the coupled model is driven by the prescribed wind from an initial control run. The method is akin to that illustrated in Ding et al. (2013) and as applied by Thoma et al., (2015) and Kovács et al. (2020) for initialization technique as they all showed skill at reconstructing the observed variability of the climate system, but applied here to the AWI-ESM and using 6-hourly winds instead of monthly mean wind stress. The Modini (extending the fully coupled climate ESM using a partial coupling technique) showed a significant skill over the period in reproducing historical climate fluctuations, indicating the potential of the method for initializing seasonal to decadal forecasts. Furthermore, some major modes of climate variability (ENSO, NAO, SAM) were reproduced as well as the response of the SST, SAT, and Sea Ice Extent (Thoma et al., 2015).

The Ocean response to the prescribed wind is the main aim of this work, thus, providing answers to the following questions on how the prescribed wind stress affect the Ocean: Is there a link between wind stress and SST? Do the Modini runs

properly simulate AMO, NAO and, Niño 3.4?. How does the Modini simulation impact the AMOC heat transport?

In the remainder of the paper, Chapter 2, I introduced the datasets, model simulations, and methodologies. The results are analyzed in Chapter 3. In Chapter 4, the possible mechanisms are proposed and discussed. Finally, a summary and discussion of the results are presented in Chapter 5.

Chapter 2

Methodology

2.1 AWI-ESM

The experiment was carried out using the newly developed AWI-ESM-2.1 comprising of ECHAM6 (Stevens et al., 2013) the atmospheric general circulation model, and FESOM-2.0, the finite volume sea-ice ocean model (Sidorenko et al., 2019). The AWI-ESM is a fully coupled global climate model that has proven to be a useful tool in providing state-of-the-art computer simulations of the Earth's past, present, and future climate states following a series of simulations that have been undertaken, ENSO (Brown et al., 2020), the mid-Holocene (Shi and Lohmann, 2016), the early-Holocene (Shi et al., 2020), and the Last Glacial Maximum (Lohmann et al., 2020).

2.1.1 Primitive Equation

The primitive equations derived as an approximation of the rotating Navier–Stokes equations (Li and Titi, 2019) are a set of nonlinear differential equations widely used in the atmosphere and ocean modeling. They use the Boussinesq approximation and hydrostatic approximation for the vertical component of the momentum, which is a valid assumption for most atmosphere and ocean model applications. They comprise the conservation of momentum:

$$\frac{\partial u}{\partial t} + u\frac{\partial u}{\partial x} + v\frac{\partial u}{\partial y} + w\frac{\partial u}{\partial z} - fv = -\frac{1}{\rho o}\frac{\partial P}{\partial x} + \frac{\partial}{\partial z}(K_e\frac{\partial u}{\partial z}) + F_u \tag{2.1}$$

$$\frac{\partial v}{\partial t} + u\frac{\partial v}{\partial x} + v\frac{\partial v}{\partial y} + w\frac{\partial v}{\partial z} - fu = -\frac{1}{\rho o}\frac{\partial P}{\partial y} + \frac{\partial}{\partial z}(K_e\frac{\partial v}{\partial z}) + F_v \tag{2.2}$$

$$\frac{\partial P}{\partial z} + \rho g = 0 \tag{2.3}$$

in the three space coordinates x, y, z; f is the Coriolis parameter; ρ is the density; P is the pressure; g is the gravitational acceleration; K_e is a coefficient for eddy viscosity and F_u and F_v represent horizontal diffusion of momentum while u, v, w are the components of velocity. Assuming an incompressible fluid, the conservation of mass:

$$\frac{\partial u}{\partial x} + \frac{\partial v}{\partial y} + \frac{\partial w}{\partial z} = 0 \tag{2.4}$$

The conservation of energy and in the case of the O cean also the conservation of salinity:

$$\frac{\partial \theta}{\partial t} + u\frac{\partial \theta}{\partial x} + v\frac{\partial \theta}{\partial y} + w\frac{\partial \theta}{\partial z} = \frac{\partial}{\partial z}(K_h\frac{\partial \theta}{\partial z}) + F_\theta \tag{2.5}$$

$$\frac{\partial S}{\partial t} + u\frac{\partial S}{\partial x} + v\frac{\partial S}{\partial y} + w\frac{\partial S}{\partial z} = \frac{\partial}{\partial z}(K_h\frac{\partial S}{\partial z}) + F_s \tag{2.6}$$

where θ and S are potential temperature and salinity, respectively; K_h is a coefficient for the thermal vertical eddy diffusion and F_θ and F_s represent horizontal thermal, and salt diffusion. And an equation of state. For the atmosphere this is:

$$P = \rho RT \tag{2.7}$$

where T is the temperature and R is the specific gas constant. For the Ocean, density is a function of temperature and salinity.

2.1.2 The Atmospheric Model ECHAM6

ECHAM is a general circulation model, and its name was coined as a merger of its origin (the 'EC' being short for 'ECMWF') and the location of development of its parameterization package ('HAM') Hamburg. The current version of ECHAM, ECHAM6 (a model program for the interactive calculation of the general circula-

tion), was developed based on ECHAM5 (Roeckner et al., 2006).

The model has been widely used for climate simulations as a stand-alone model with prescribed lower boundary conditions but also coupled with dynamical ocean models, and it contributed to the Coupled Model Intercomparison Project (Sidorenko et al., 2015). Radiative transfer in ECHAM6 is represented by the rapid radiation transfer (Iacono et al., 2008) containing a Land-Surface Model (JSBACH) which includes 2 bare-surface types and 12 functional plant types of the dynamic vegetation (Loveland et al., 2000; Raddatz et al., 2007). For the Alfred Wegener Institute Climate Model (AWI-CM), the T63 L47 configuration is used, which corresponds to a horizontal resolution of about 1.85°x 1.85°and 47 vertical levels with the top-level at 0.01 ha. A detailed description can be found in Stevens et al. (2013).

2.1.3 The Ocean and Sea Ice Model FESOM2.0

FESOM2.0 used for this experiment is a global ocean general circulation model developed at Alfred Wegener Institute, Helmholtz Centre for Polar and Marine Research AWI. FESOM2.0 is based on finite volume discretization which is formulated on unstructured meshes and offers multi-resolution functionality in faultless and flawless ways. The multi-resolution approach advocated by FESOM is successful and allows one to explore the impact of local processes on the global Ocean with moderate computational effort (Danilov et al., 2017). In a bit to explore ways to further increase the numerical efficiency of unstructured mesh and extend their area of applicability, FESOM2.0 was developed.

FESOM consists of a 3D Ocean circulation model and a 2D sea-ice model. The Ocean circulation model solves the hydrostatic primitive equations with Boussinesq and traditional approximations splitting the set of equations into a dynamical and thermodynamic part (Danilov et al., 2004). All 3D variables are stored as 2D arrays with vertical and horizontal extents, thereby splitting long cycles over elements and nodes, as well as over vertical layers. Therefore increasing its numerical efficiency and subsequently its performance which is close to that of a structured mesh (Danilov et al., 2017). The performance of FESOM2.0 is compared to that of FESOM1.4 in simulation-driven by the CORE-II forcing (Large and Yeager, 2009),

reports have it that the simulations carried out on a coarse mesh used by FESOM1.4 in the framework of CORE-II inter-comparison and on global mesh with a resolution of about 15km, illustrating it to be a fully functional and highly competitive general ocean circulation model. This new version improves the numerical efficiency of FESOM in terms of the central processing unit time by at least 3 times while retaining its fidelity in simulating sea-ice and the ocean. A detailed description of the physics of the sea-ice model FESOM2.0 can be found in Danilov et al. (2017) and Sidorenko et al. (2019).

2.1.4 OASIS

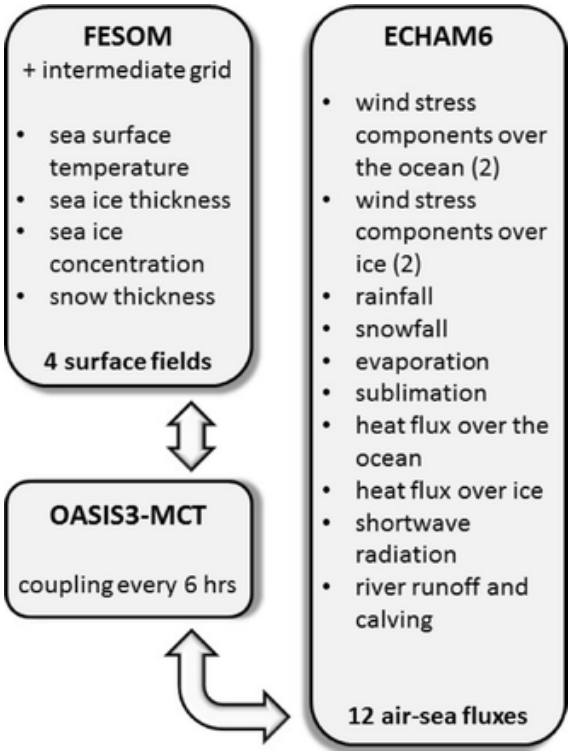

Figure 2.1: Coupling procedure within AWI-ESM. The six-hourly averaged fields are mapped between the model components employing an intermediate exchange grid (Sidorenko et al., 2015).

To exchange data between the different models, the output data of one model has to be converted in such a way, that it can be read into the following model. The coupling mechanism implemented in AWI-ESM is the OASIS3-MCT coupler. It was used in this project in the coupling between ECHAM6 and FESOM2.0. The major function of the OASIS3-MCT is to interpolate as well as exchange coupling fields to

create a coupled system. This is achieved after compilation because OASIS3-MCT is a coupling library that is connected to the component models. As both models use different grids, the coupling must take care of fitting one model's data into the other model's grid. This is done by mapping the data on an intermediate grid. The mapping from this grid on the unstructured FESOM mesh is carried out by FESOM itself, while the mapping from the intermediate grid on the atmospheric grid is done by the coupler using bi-linear interpolation. A detailed description of the coupling is given in Sidorenko et al. (2015). Figure 2.1 shows the coupling procedure.

2.2 Modini Method

The fully coupled climate model, Alfred Wegener Institute Earth System Model (AWI-ESM) was extended using a partial coupling technique (Modini). This method is implemented by prescribing wind forcing from the AWI-ESM fully coupled control run to the AWI-ESM's inherent climatological wind field when computing the surface wind stress that drives the Ocean and sea-ice model. In the case of reanalysis wind forcing, anomalies are used instead of the full wind field to reduce potential model drifts due to different mean climate states of the unconstrained AWI-ESM and the partially coupled Modini, which could arise if total observed wind stress was used (Thoma et al., 2015). However, for this study, I have engaged the full wind field since I have used the same model and environment for the fully coupled run and the partially coupled run. The method is akin to the description in Ding et al. (2013) but applied here to the AWI-ESM and using 6-hourly winds as carried out by Thoma et al. (2015) instead of monthly mean wind stress anomalies as used by Ding et al. (2013). It should be noted that SST is computed using the coupled model physics and is indirectly constrained in the partially coupled model. Likewise, ECHAM6 computes its wind field and only knows about the time series of events through the SST and all other variables that are coupled to the atmosphere that is given to it by the Ocean model and the influence of the specified radiative forcing. The primary aim of the Modini was to spin up and launch a coupled climate model for decadal forecasts. Besides this purpose, the indirect response of

the atmospheric circulation can be stimulated by the Modini as an experimental tool to prescribe wind forcing coherently, as long as the remnant of the coupling remains the same as in the initial configuration. The simulation of the oceanic and atmospheric properties in connection with the climate's internal variability was skillfully demonstrated by Ding et al., 2013; and Thoma et al., 2015. A very recent implementation of the Modini method can be found in Kovács et al. (2020).

2.2.1 Experimental Design and Spinup Strategy

Two different models set up have been used for this work, the AWI-ESM, and the FESOM Standalone. Two FESOM Standalone models were forced by the 6-hourly atmospheric reanalysis dataset CORE-II (Large and Yeager, 2009) ranging between 1948–2009 and were initialized with the Polar Science Center Hydrographic Climatology (PHC3) (Steele et al., 2001). A spinup time of about 300 years is needed to bring the upper and intermediate Ocean into a quasi-equilibrium state as shown in previous studies by Sidorenko et al., (2011), Wang et al., (2012), and Scholz et al., (2013). Thus, five successive spinup cycles each with a length of 62 years to reach a quasi-equilibrium model state consecutive were carried out. For every spinup cycle, the last output of the preceding spinup was introduced as a new initialization as suggested in the CORE-II protocol (Danabasoglu et al., 2014) and applied in other ocean modeling studies (Lohmann et al., 2009; He et al., 2016; Karspeck et al., 2017; Danek et al., 2019). It is imperative to state here that all the runs were performed with the AWI-ESM except the UCOREII and WCOREII that were carried out with the FESOM Standalone.

Table 2.1: Simulation table. The forcing columns show the runs forced by prescribed wind stress settings (partially coupled) or fully coupled with their respective CO_2 levels for CMIP6.

Experiments	**Prescribed wind**	**Forcing CO_2 Level**	**Year**	**Restart**
Preindustrial (PI)	NO	277.15ppm	1750-2100	1750
Partially Coupled PI (PCPI)	YES	284.32	1850-2100	1850
Fully Coupled Historical (HIST)	NO	284.32	1850-2014	1850
Partially Coupled Historical (HIST1)	YES	284.32	1850-2014	1850
Fully Coupled Future (FUT)	NO	397.55	2015-2100	2014
Partially Coupled Future (FUT1)	YES	397.55	2015-2100	2014
Unperturbed COREII Forcing (UCOREII)	NO	NIL	1948-2009	2009
Perturbed COREII Forcing (WCOREII)	YES	NIL	1948-2009	2009

The simulated runs for this experiment for notational simplicity are as seen in the table above. The wind stress of the WCOREII has been multiplied by a factor of 1.5, thus it is called the perturbed FESOM standalone run while the UCOREII is unperturbed. The simulations were based on a fully AWI-ESM 2.1 run that used the same setup and greenhouse gas forcing as the historical run until 2014. The future scenarios are based on the Shared Socio-Economic Pathway585 (SSP585) emission. The source of the prescribed wind for computing the stress was derived from the fully coupled control run. I took the zonal and meridional wind forcing from the last 30 years of my fully coupled control simulation and read them in repeatedly while extending my fully coupled run hence, known as partially coupled runs of the respective fully coupled run. The wind stress field was read every 30 minutes. The Ocean model component FESOM2.0 is driven by wind stress based on a prescribed wind field using the Modini method while the atmospheric model component ECHAM6 computes its field accordingly to the fully coupled dynamics maintaining its consistency with heat and energy exchange. The differences between each sensitivity experiment and Control runs are regarded as the anomaly.

2.3 Experiment Evaluation

To investigate the response of the Ocean to wind forcing using the partially coupled Modini method, we considered time-dependent Climate indices for the direct Ocean and indirect atmosphere in both hemispheres with a keen interest in the North Atlantic region. The results of the fully coupled models were compared and contrasted with that of the equivalent partially coupled model. Also, the results of the Standalone outcomes were compared.

2.4 Indices

Different computational indices were used for this study as suggested by previous studies.

The AMO Index

The AMO indices used in this paper are constructed based on the simulated SSTs in a similar way following previous studies (Sutton and Hodson, 2005; Knight et al., 2006; Trenberth and Shea, 2006; Dima and Lohmann, 2007). Each index is calculated by averaging the annual mean SST over the region 0°N-60°N, 80°W-0°E. All the indices are detrended after which the monthly averages were calculated for the last 30 years for each simulation, then normalized by subtracting the monthly average from the original file to obtain the difference, i.e., an anomaly. Finally, the AMO index is obtained by applying a 5-yr (60-month) running mean filter to this time series to remove interannual and seasonal variability.

A roughly 0.4°C peak-to-peak oscillation can be obtained from a 60-month running mean of each index. This is in good agreement with the observed AMO variation albeit with a 25-year running mean (e.g., Dima and Lohmann (2007)). The AMO warm and cold periods are depicted in Fig. 2.2a

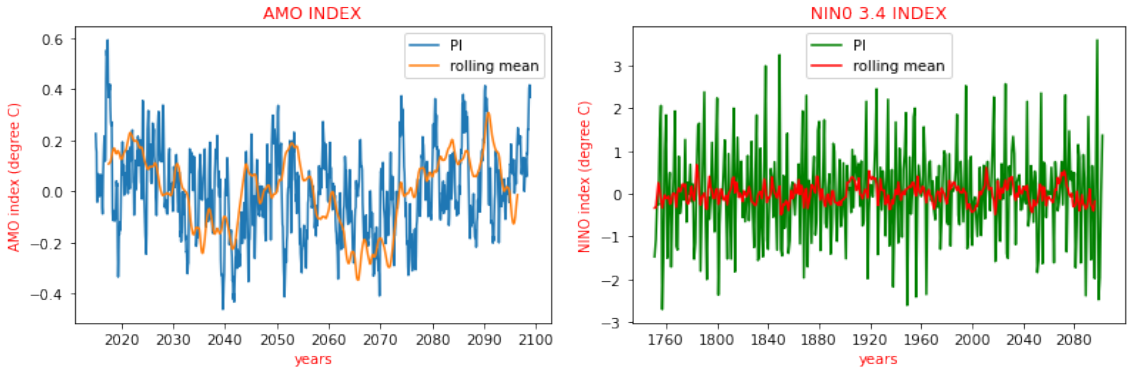

(a) (b)

Figure 2.2: Computational indices used for this paper: (a) The AMO Time series for the fully coupled pre-industrial run (PI) in blue with the running mean value in yellow. (b) The Niño 3.4 Time series for the fully coupled pre-industrial run (PI) in green with the running mean value in red.

The Niño 3.4 Index

Defining the ElNiño or ElNiño event has been difficult as some scientists define it in terms of coastal phenomenon confinement while others view it from the basin-wide perspective whereas, the layman sees no distinction in both views (Trenberth, 1997).

The argumentation and validity of the preferred view of definition is however not the focus of this paper but the used index. There are various indices of ElNiño as discussed in Trenberth (1997) but the Niño 3.4 index which is one of the most commonly used indices has been used for this research work. It is determined as SST anomaly averaged over the region, 5°N - 5°S, 170°W - 120°W. A 7-month running mean was introduced to smooth out intra-seasonal variations of the SST anomalies in the tropical Ocean. The periods that qualify depict the El Niño years and provide a quantitative measure of the intensity as shown in Fig.2.2b. A detailed explanation of Niño 3.4 can be found in Trenberth (1997).

The NAO Index

The NAO index can be defined as the difference in sea-level atmospheric pressure between Azores High and Iceland Low (Hurrell, 1995). The NAO index is defined also as the time series corresponding to the first Empirical Orthogonal Function

mode of sea level pressure over the North Atlantic region (Hurrell and Dickson, 2004). The NCAR Command Language (NCL) was used to compute the first EOFs of the NAO.The NAO is obtained from sea level pressure, which is changing much faster than the sea level temperature. This is the main cause for why many methods struggle with these indices (Norel et al., 2021).

In this paper, the NAO index (NAOI) has been computed with the most frequently used mathematical description of the NAO phase. The NAO index is calculated by taking the difference between normalized surface pressure anomaly from a 30-year mean of the Azores High and the Icelandic Low. The drawback of this proxy is that it does not account for the fluctuations in the stated locations. This implies that the NAO station-based index partially captures the seasonal, interannual, and multidecadal spatial variability in the North Atlantic pressure patterns (Hanna et al., 2015).

$$NAOI = \frac{P_H - P^*_{H30years}}{std(P_{H30years})} - \frac{P_L - P^*_{L30years}}{std(P_{L30years})} \tag{2.8}$$

P_H is the mean monthly SLP for Azores High while P_L is that of the Icelandic Low and P^* being the mean value. The 30 years average of every corresponding month's SLP is used and std means the corresponding month's monthly standard deviation. As explained in Hurrell (1995).

Chapter 3

Results and Analysis

To investigate the differences arising from the fully coupled and its counterpart partially coupled simulations, the period is chosen to be the same except for the control simulations which are longer than the PCPI. The variations of all the indices obtained from all data sets used in terms of their calculations are generally consistent.

To estimate the ability of the partially coupled Modini-AWI-ESM-2.1 to track the time evolution of the observed climate system compared to the fully coupled Earth system model AWI-ESM-2.1, we consider several spatial and/or time-dependent climate indices for Ocean and Atmosphere, in both hemispheres. For each of these control variables, the results of the fully coupled AWI-ESM–2.1 experiment are compared with the equivalent Modini-AWI-ESM-2.1 outcomes.

3.1 Atlantic Multidecadal Oscillation

In Fig. 3.1, the different simulations with AMO indices portray decadal and multi-decadal variability of warm and cold periods connected with variations in the AMO. We can distinguish the effects of the prescribed wind stress as the trends of the fully coupled and partially coupled runs are very unique. Both the fully coupled and partially coupled models simulate the AMO remarkably well but with the partially coupled models having higher amplitude. The PCPI in Fig. 3.1a shows higher amplitude than the PI in response to the prescribed wind stress.

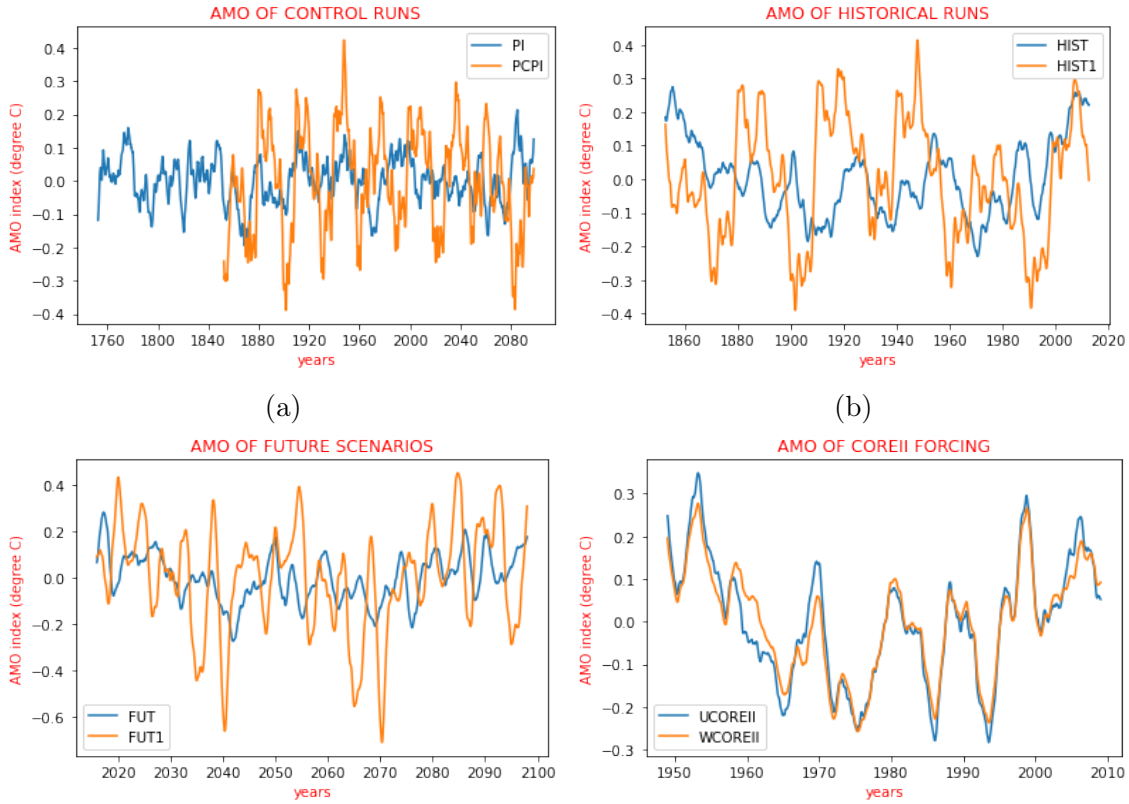

Figure 3.1: The AMO Time series for: (a) the control run (PI) and the partially coupled pre-industral run (PCPI). (b) the fully coupled historical (HIST) and the partially coupled historical run (HIST1). (c) the fully coupled SSP585 scenario (FUT) and partially coupled SSP585 simulation (FUT1). (d) the unperturbed (UCOREII) and perturbed (WCOREII) FESOM standalone forcing at quasi equilibrum state. The AMO index is a computation of detrended 60-month low-pass filtered average SSTs across the area (0°N-60°N, 80°W, 0°E) (Trenberth and Shea, 2006).

For the COREII forcing in Fig. 3.1d the models are also well represented in inter-

annual and decadal variability in a similar way seemingly indistinguishable as the unperturbed UCOREII forcing and the perturbed WCOREII forcing practically display the same variation trend, howbeit with slight amplitude of UCOREII edging out that of WCOREII. This is expected because I prescribed SST (and other surface conditions) in Ocean. The partially coupled models are all weakly correlated with the fully coupled models for 95% confidence level of the Pearson's Correlation. The full correlation table is given in Table A.1. A prominent decrease from 1960 in Fig. 3.1b (HIST1 and HIST for AMO) might indicate that volcanic eruptions have significant impacts on the AMO. A proper representation of other atmospheric forcings like stratospheric aerosols and ozone might also have played a role here. However, it is seen that all the factors affecting the future scenario like the GHG are enhanced by the winds tress with larger amplitudes in Fig. 3.1c.

3.2 Niño 3.4

In Fig. 3.2a, the partially coupled run simulates the ENSO variability remarkably well and captures almost all of the ENSO events as well as the fully coupled models. The amplitudes are also higher in the PCPI than that of the PI in most ENSO events, as the ocean coupling leads to a dampening of the Niño 3.4 amplitudes. The same observation is evident in Fig. 3.2b and Fig 3.2c, however with some drifts perhaps as a result of the internal variability of the AWI-ESM.

These drifts are much more profound in the future scenario runs in Fig. 3.2c, which might also suggest the presence of GHGs corrupting the internal variability of the model. There is relatively no correlation between the FUT and FUT1 as the Pearson correlation between them is -0.01.

The FESOM Standalone in Fig 3.2d shows the same pattern but with the unperturbed UCOREII expressing higher amplitudes. The WCOREII is fully relegated to the background dominated by the UCOREII with a higher amplitude indicating that the stronger the wind stress, the lower its amplitude. However, the WCOREII, has very minimal amplitudes and is unable to capture the timescales of the observed Niño3.4 index. Thus, the nearly-flat thick red line gives no information on ENSO.

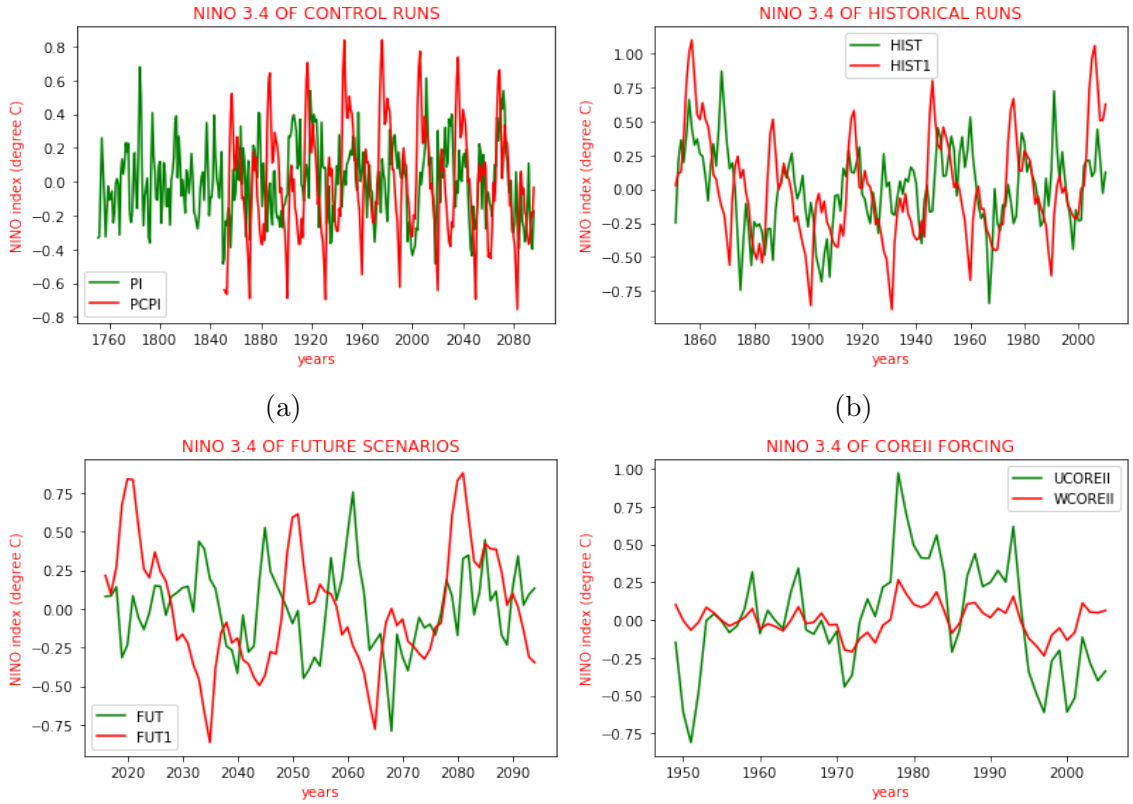

Figure 3.2: The Niño 3.4 Time series for the: (a) control run (PI) and the partially coupled pre-industral run (PCPI). (b) fully coupled historical (HIST) and the partially coupled historical run (HIST1). (c) the fully coupled SSP585 scenario (FUT) and partially coupled SSP585 simulation (FUT1). (d) unperturbed (UCOREII) and perturbed (WCOREII) FESOM standalone forcing at quasi equilibrum state. The Niño 3.4 index is a computation of detrended 7-month low-pass filtered average SSTs across the area (5°N-5°S, 170°W-120°W) (Trenberth, 1997).

3.3 North Atlantic Oscillation

The NAO spatial pattern for the first EOF of the SLPs are as shown in Fig 3.3, there is the various period of phase transitions. The movement of action centers of the NAO can be seen when comparing the fully coupled and partially coupled runs. In the PI run (Fig. 3.3a), the low-pressure action center is more pronounced and at around 40°W. The reverse is the case for the PCPI (Fig. 3.3b), as the high-pressure action center is more pronounced and at around 30°W. For the historical experiments, the high- and low-pressure action centers are obvious but also different as seen in Fig. 3.3c. The more pronounced high-action center drifts towards the equator while the less pronounced low-action center is around 40°W. Meanwhile as the low-action center reduces in strength, its corresponding high-action center is strengthened (Fig. 3.3d). In Fig. 3.3e, the FUT depicts the low-pressure action center at around 45 °W with a much less pronounced high-pressure action center. In a similar trend as with the partially coupled runs, the high-pressure action center is very pronounced and at around 10 °W closing into the equator. However, the low-pressure action center is less pronounced (Fig. 3.3f). Hence, signifying the overwhelming effect of the partially coupled to the fully coupled simulations due to the effect of the wind forcing.

The bar chart plots using the station based method show slightly evenly distributed positive and negative NAO phases but with prominent exceptions as in the years 1760-1820 and 1850-1920 which can be referred to as the negative phases of the PI while 1820-1850 and 1920-1980 can be regarded as its positive phase in Fig 3.3a. The very obvious phase transition that can be termed as the negative in Fig. 3.3b is 1880-1900 and 2010-2020. This is in tandem with the spatial first EOF as shown above in the bar chart plots. The same trend is evident in the HIST and HIST1 as seen in Fig. 3.3c and Fig. 3.3d respectively. There is a more pronounced positive phase than the negative phase. Prominent positive phase periods 2015-2025 and 2060-2065 can be seen in the FUT experiment in Fig. 3.3e while the profound negative phase period is around 2050-2060. Furthermore, the FUT1 in Fig. 3.3f shows 2025-2035 and 2055-2070 are prominent periods in the negative phase, while

2040-2055 and 2070-2080 are prominent periods in the positive phase.

In Fig. 3.4a, interannual variations are noticed in the PI and PCPI but largely exhibited in the PI. The partially coupled run has fluctuating amplitudes, edging out the fully coupled run from most of the intervals leading to a larger variation. The PCPI proceeded from the negative rising to a peak of about 2hPa before maintaining almost the same trend with similar peaks with the PI at the mid 21st century. The prominent peaks depicting profound decadal variations in the PCPI are between 1890-1950-2025, signifying the occurrence of the peaks around 60-75 years. In Fig. 3.4b, the fully coupled historical simulation shows interannual and decadal variations, however mildly between 1 and -1 in amplitude until the last decade of the 19th century when it experiences a major decline in the negative phase until -2 hpa. The HIST1 on the other hand exhibits the opposite trend to the HIST up until 1960 with its maximum peak at 2 and its minimum at -3, indicating how the wind forcing strengthens the HIST1. The role of the wind stress in the NAO time series in Fig. 3.4c is not very pronounced as FUT and FUT1 almost maintained a similar trend all through.

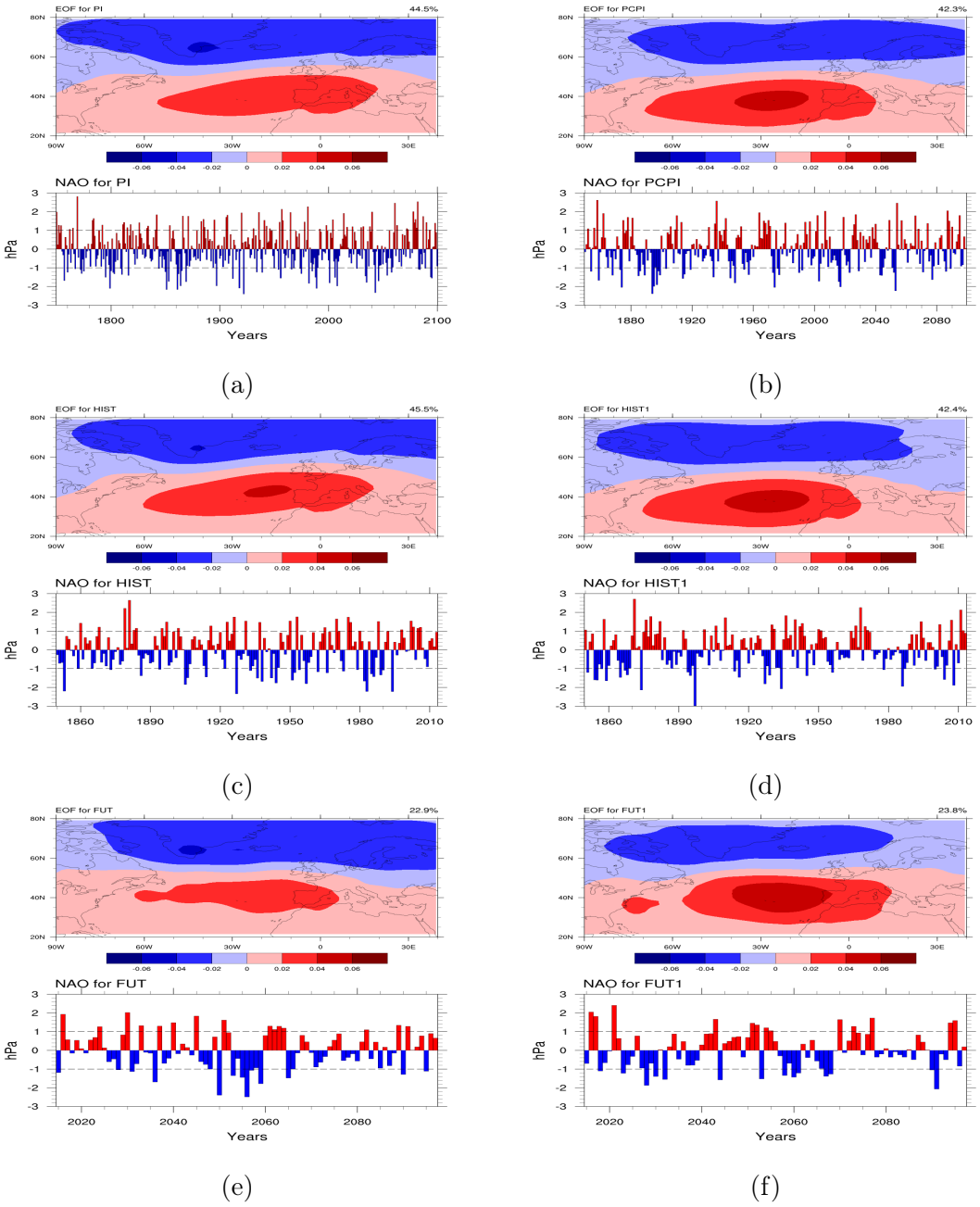

Figure 3.3: (a) The NAO mode of observation based SLP for winter (DJF) with its corresponding bar chart time series for the fully coupled pre-industrial run (PI). (b) as in (a) but for PCPI. (c) as in (a) but for HIST (d) as in (a) for HIST1 (e) as in (a) but for FUT (f) as in (a) but for FUT1.

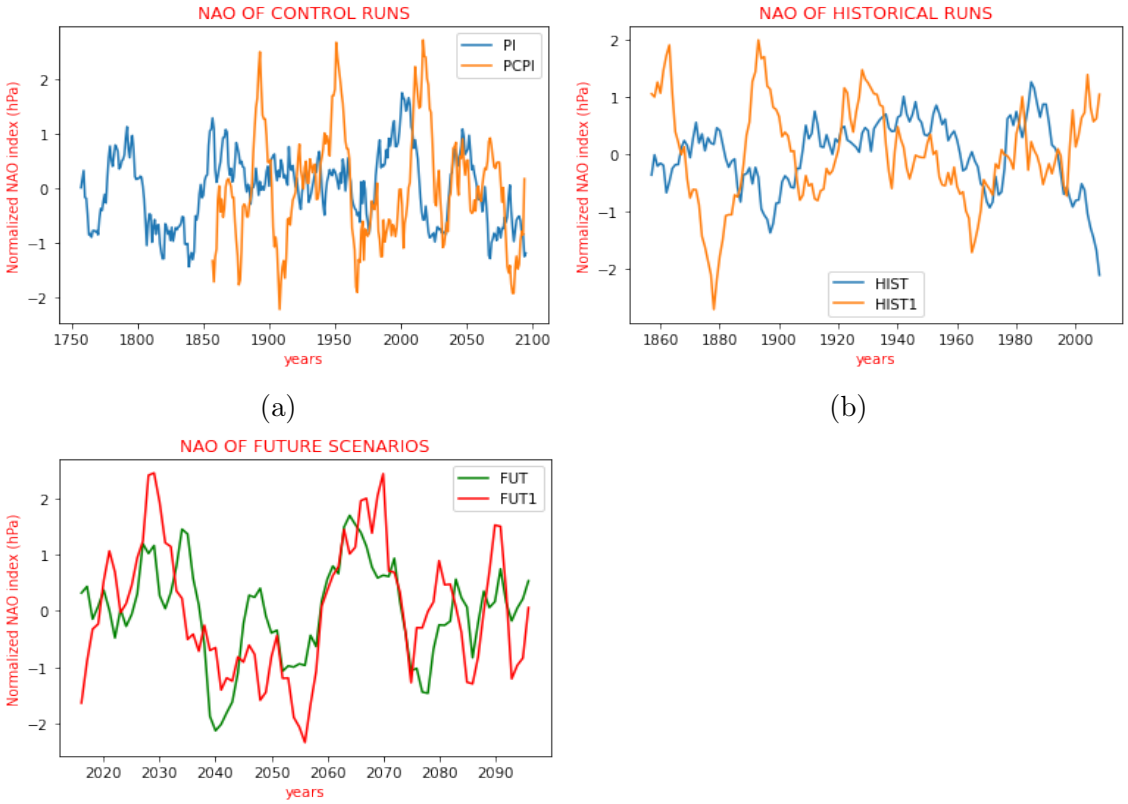

Figure 3.4: The NAO Time series for the: (a) fully coupled pre-industrial run (PI) and the partially coupled pre-industral run (PCPI). (b) fully coupled historical (HIST) and the partially coupled historical run (HIST1). (c) fully coupled SSP85 scenario (FUT) and partially coupled SSP585 simulation (FUT1). The NAO index is defined as the normalized SLPs difference between the Azore High and Icelandic Low (Hurrell, 1995), with detrended 15-year low-pass filtered annual mean area-averaged SLP anomalies over the North Atlantic region 70°W–20°E and 20°N–80°N.

3.4 Atlantic Meridional Overturning Circulation

The AMOC indices are derived from the maximum meridional stream function at a 1000-m depth of 26.5°N in the Atlantic Ocean i.e. the AMOC strength is defined as the maximum of the overturning stream function in the Atlantic Ocean in which the AMOC features are evaluated at 26.5°N. The introduction of surface wind forcing can affect the AMOC significantly. In the control PI run, the AMOC strength is around 16.5 Sv and its trend is maintained showing interannual and decadal variations. The AMOC is weakened quickly at the initial stage when the surface wind is introduced in the North Atlantic (PCPI) after which momentum is gained as it fluctuates depicting interannual and decadal variations attaining its maximum amplitude at about 30 Sv as seen in Fig. 3.5a, the preindustrial runs. The trend in the AMOC seems to remain the same as there is a predominantly increment in the amplitude of the PCPI. The equilibrium response of the PCPI AMOC is about 7 Sv reaching a quasi-equilibrium state in 50 years.

The AMOC in the HIST is also practically maintained as seen in Fig. 3.5b with the AMOC strength of about 17.5 Sv showing interannual and decadal variations. The AMOC is massively weakened with the addition of the surface wind forcing with an initial strength of 10 Sv in the HIST1. After about 40 years and 12.5 Sv, a quasi-equilibrium is attained. After which the THC trend is maintained all through to 1940 before another slight increment in strength is observed in 1970.

In Fig. 3.5c There is a continuous decline for the FUT with an AMOC strength of about 16.2 Sv. The AMOC strength of FUT1 also maintains a downward trend howbeit showing interannual and multidecadal trends with prominence between 2045 and 2075 for the FUT1.

The UCOREII depicts interannual and decadal variations with an AMOC strength of about 11.5 Sv with a maintained THC as seen in Fig. 3.5d. The strength of the WCOREII is 38 Sv, which is more than three times the UCOREII. There is an upsurge in the amplitude after 1970 and a further decline after 1990 indicating that there are external forcings included as the forcing changes over time. In all the models there seems to be stability in the fully coupled AMOC as well as

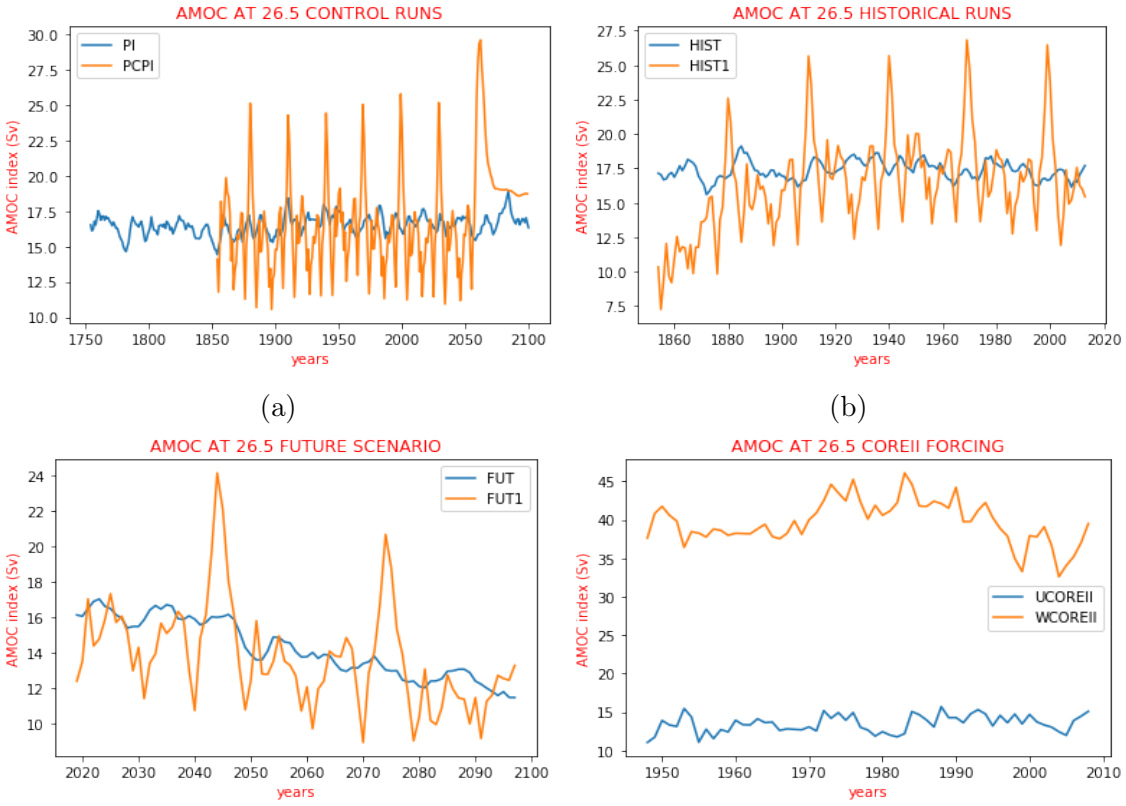

Figure 3.5: The monthly values of AMOC 26.5°N Time series [in Sverdrup, 1 Sv = 10^6 m^3/s] with a rolling mean of 7 months for the: (a) fully coupled preindustrial run (PI) and the partially coupled preindustrial run (PCPI). (b) fully coupled historical run (HIST) and the partially coupled historical (HIST1). (c) fully coupled future scenario run (FUT) and the partially coupled future scenario run (FUT1). The future scenario run indicates the SSP585. (d) unperturbed FESOM standalone forcing (UCOREII) and perturbed FESOM standalone forcing (WCOREII) multiplied with a value of 1.5.

the unperturbed COREII forcing AMOC except for the FUT (as it maintains a downward trend). Significant weakening of the AMOC is conspicuous in the FUT1 and WCOREII around 1997.

Fig. 3.6a shows the vertically integrated stream function for the control run, i.e. under fixed preindustrial conditions having the maximum of about 16 Sv at 1,000 m depth of 26.5°N. As positive values indicate a clockwise current, there is a strong upper cell at a depth of around 1,000 m. This cell transports water masses northward, returning at an intermediate depth to the south. There is also a weak lower cell at around 4,000 m. This cell consists of Antarctic Bottom Water (AABW), flowing from south to north. It shows that the AABW cell reaches out to around 35°N.

The AMOC anomaly in Fig. 3.6b, the partially coupled preindustrial stream function shows that there is a gain of about 3 Sv at 1000m depth after which there is a massive decrease of about 4 Sv, with the AABW rising to about 1,000 m with the minimum of 4 Sv at 2,000 m depth. For the Historical models, the AABW rises to about the depth of 2,500 m at 26.5°N as seen in Fig. 3.6c and Fig. 3.6d, with prominent AABW evident in the HIST1 anomaly stream function. There seems not to be any apparent strong upper cell in the future scenario runs (FUT and FUT1) (Fig. 3.6e and Fig. 3.6f) even as the FUT1 anomaly depicts enormous AABW. This shows the weakening in the AMOC as seen in the HIST and HIS1 Fig. 3.6c and Fig. 3.6d.

Fig. 3.7a looks pretty much like Fig. 3.6a indicating a stronger upper cell around 1000m and of course a weak lower cell of about 4000m. But the Fig. 3.7b depicts a very strengthened upper cell indicating the massive transport of water masses northward at a rapid rate with the lower cells almost overridden by positive values indicating the massive strengthening of the AMOC by the enhanced wind stress.

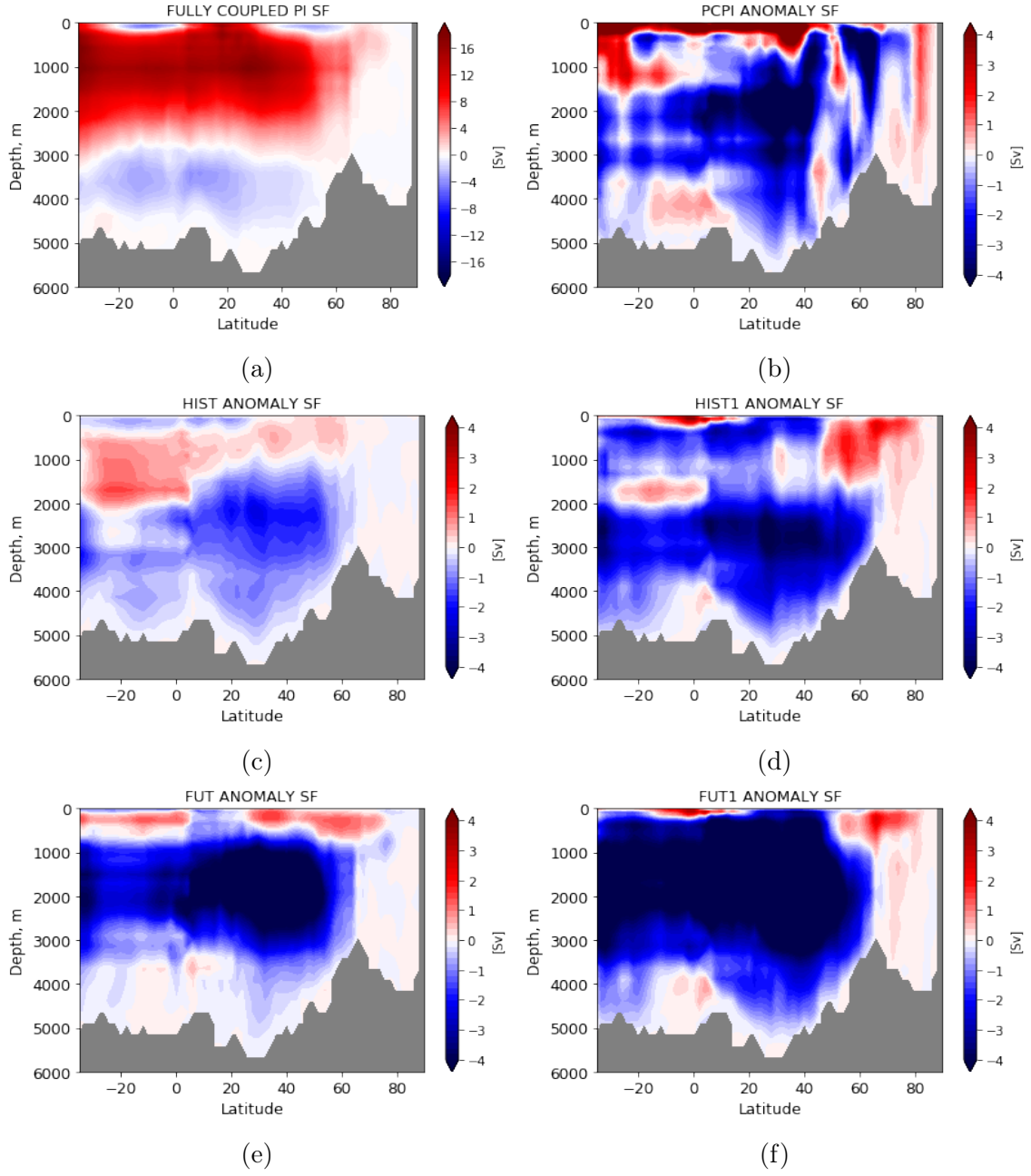

Figure 3.6: (a) The 30-year mean (2071-2100) of the stream function under preindustrial conditions. Positive values indicate clockwise current, negative values a counter-clockwise current. (b) The 30-year mean anomaly (2071-2100) of the stream function for PCPI. (c) The 30-year mean anomaly (1985-2014) of the stream function for Historical run. (d) as in (c) but for HIST1 (e) The 30-year mean anomaly (2069-2098) of the stream function for FUT. (f) as in (e) but for FUT1. [All in Sv].

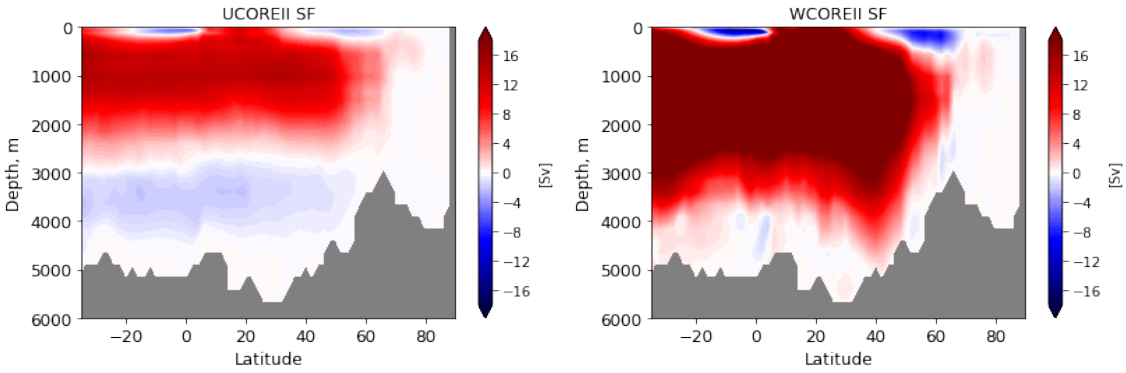

(a) (b)

Figure 3.7: (a) The 30-year mean (1980-2009) of the AMOC stream function under unperturbed FESOM standalone forcing (UCOREII) condition. (b) The 30-year mean (1980-2009) of the AMOC stream function under perturbed FESOM standalone forcing (UCOREII) condition with a multiplying factor of 1.5. [All in Sv] .

3.5 Wavelet Analysis

To further analyze the influence of the prescribed wind stress on the examined variability mechanisms, the wavelet analysis is introduced to examine the spectral occurrences of these said mechanisms.

The strong response of the wavelet transform for a particular time point and a particular frequency are indicated by the bright colours. Darker colours mean a low contribution of a frequency at a given time point. The white contour is the 5% significance level, using a white-noise background spectrum. The black lines are ridges indicating domains with high energy.The average power spectra showing more variability are in the appendix. The red dots are significant indicators for the 5% significant level for the average wavelet power using a white noise background spectrum.

In Fig. 3.8a, the wavelet spectrum for the fully coupled PI, sizeable high energy areas in the spectrum shows large multidecadal variability essentially detected in the energy bands 32-64 years with peaks around the 60 years band as indicated by the bright colour. A similar trend is observed in Fig 3.8b, the PCPI spectrum but with decreased variability and more pronounced energy occurring at 16-32, 32-64, and 64-126 years band. The wavelet spectrum for HIST in Fig. 3.8c, also shows multidecadal variability with high energy seen in 32-64 year band and 64-128 year band. Whereas less variability is found in Fig. 3.8d, high energy bands are observed just as in HIST but also at the 16-32 years band. For the FUT and FUT1 in Fig. 3.8e and Fig. 3.8f respectively, the high energy areas are seen in 16-32 and 32-64 years band, albeit with reduced variability in the FUT1.

Interannual and decadal variability is evident in the wavelet spectra for Niño 3.4 in Fig. 3.9. The PI with high energy in bands 2-4 and 4-8 years in Fig. 3.9a has higher variability than its partially coupled PI counterpart in Fig. 3.9b. Between bands 2-4 and 4-8 years, a concentration of high energy is witnessed in Fig. 3.9c as well as in Fig. 3.9d, the Niño 3.4 HIST, and HIST1 respectively but with less variability in HIST1. For the FUT and FUT1 in Fig 3.9e and Fig 3.9f respectively, a higher frequency band is observed for the FUT1 spectrum.

The PI and PCPI of the NAO wavelet spectra are very alike showing interannual variability with high energy in 2-4, 4-8, and 8-16 years band as seen in Fig. 3.10a and Fig 3.10b. The same trend is observed in Fig 3.10c and Fig 3.10d. The effect of the wind stress is not evident in the wavelet spectrum for NAO.

Just as in the case of the AMO and Niño 3.4, the wavelet spectrum for the COREII forcing as seen in Fig 3.11 shows no obvious distinguishable effect of the wind stress.

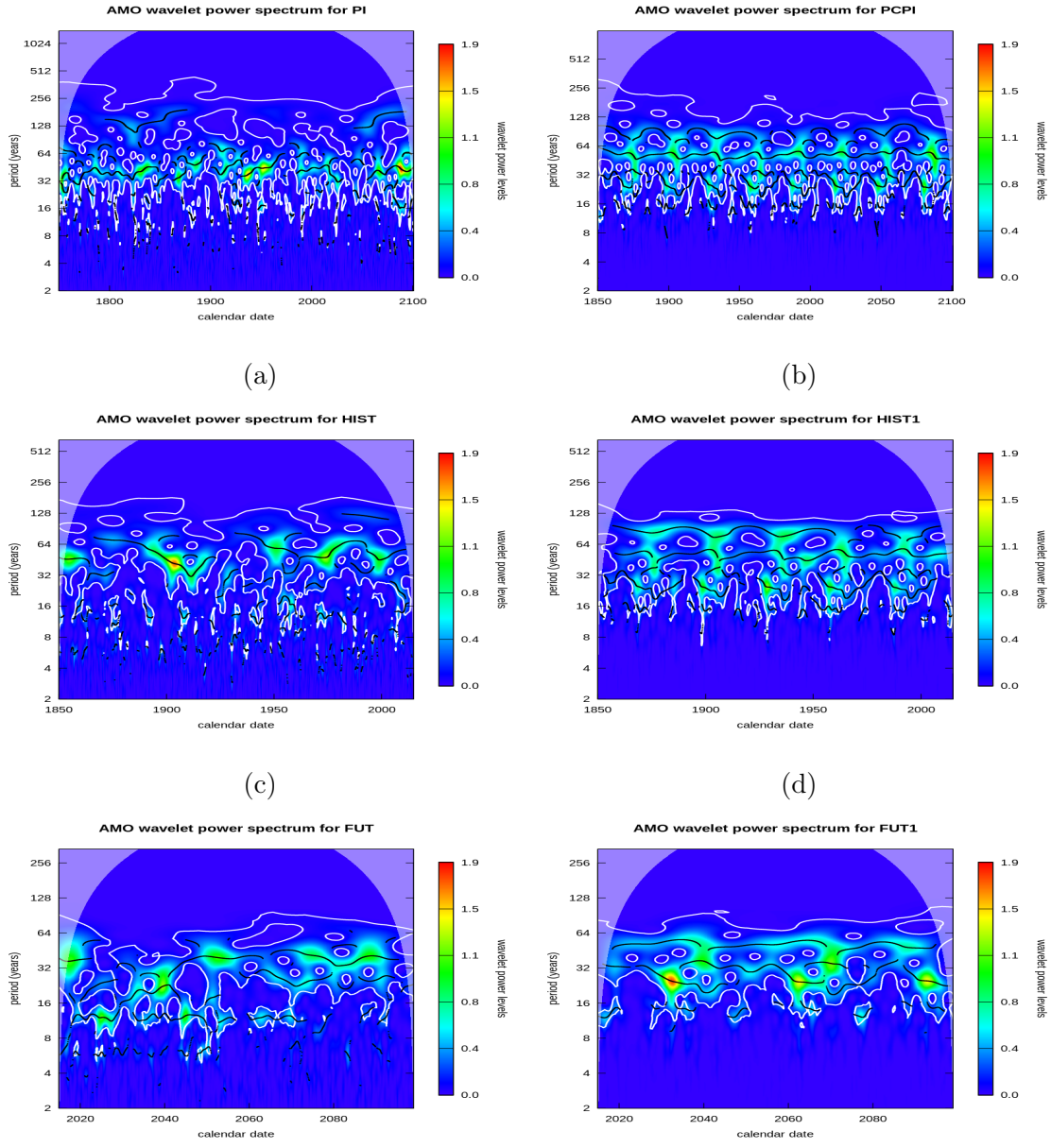

Figure 3.8: (a) The AMO Wavelet power spectrum of the fully coupled preindustrial run (PI). (b) as in (a) but with prescribed windstress of 30 years (PCPI). (c) The AMO Wavelet power spectrum of the fully coupled historical run (HIST). (d) as in (c) but with prescribed windstress of 30 years (HIST1). (e) The AMO Wavelet power spectrum of the fully coupled SSP585 run (FUT). (f) as in (e) but with prescribed windstress of 30 years (FUT1).

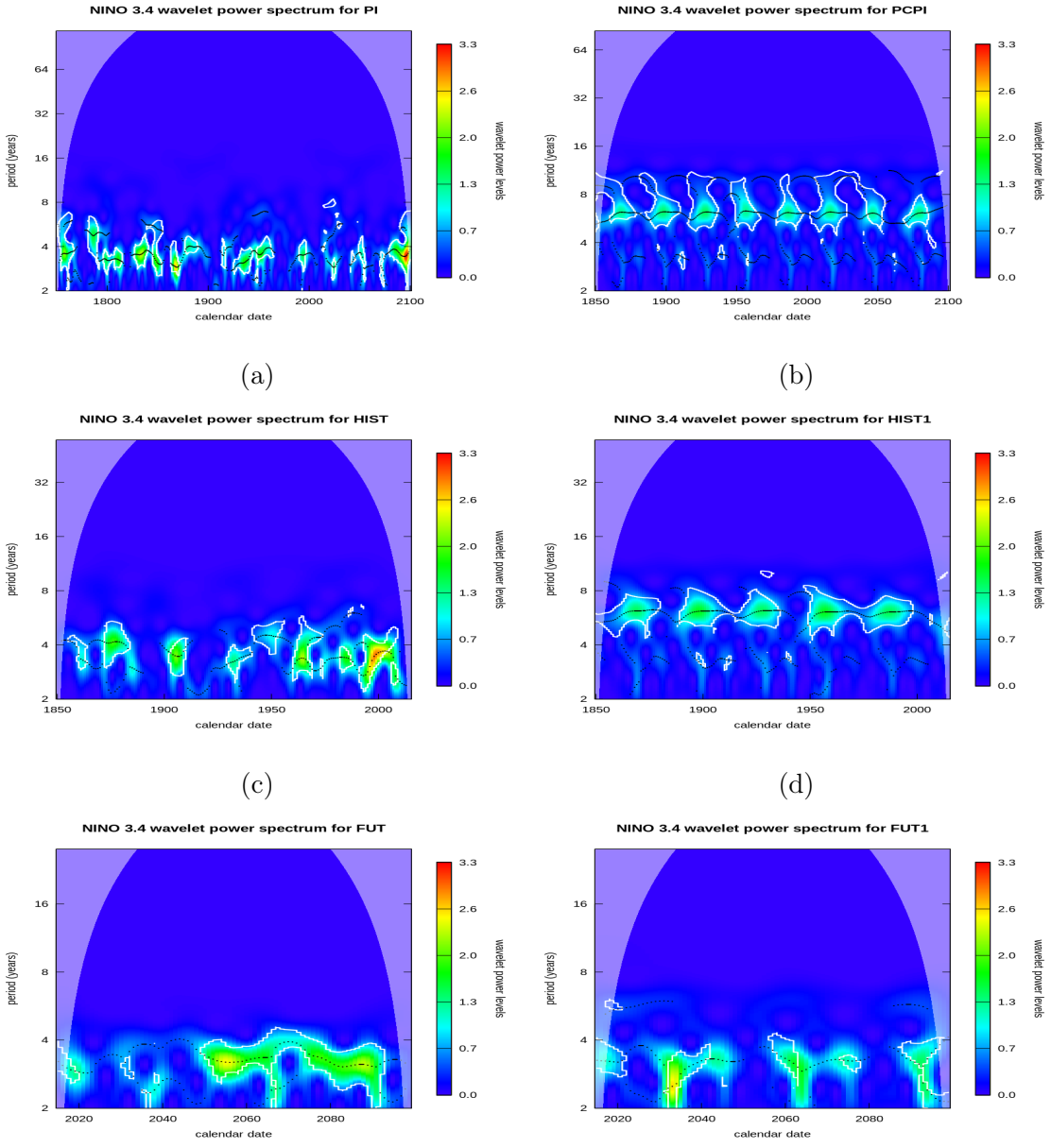

Figure 3.9: (a) The Niño 3.4 Wavelet power spectrum of the fully coupled preindustrial run (PI). (b) as in (a) but with prescribed windstress of 30 years (PCPI). (c) The Niño 3.4 Wavelet power spectrum of the fully coupled historical run (HIST). (d) as in (c) but with prescribed windstress of 30 years (HIST1). (e) The Niño 3.4 Wavelet power spectrum of the fully coupled SSP585 run (FUT). (f) as in (e) but with prescribed windstress of 30 years (FUT1)

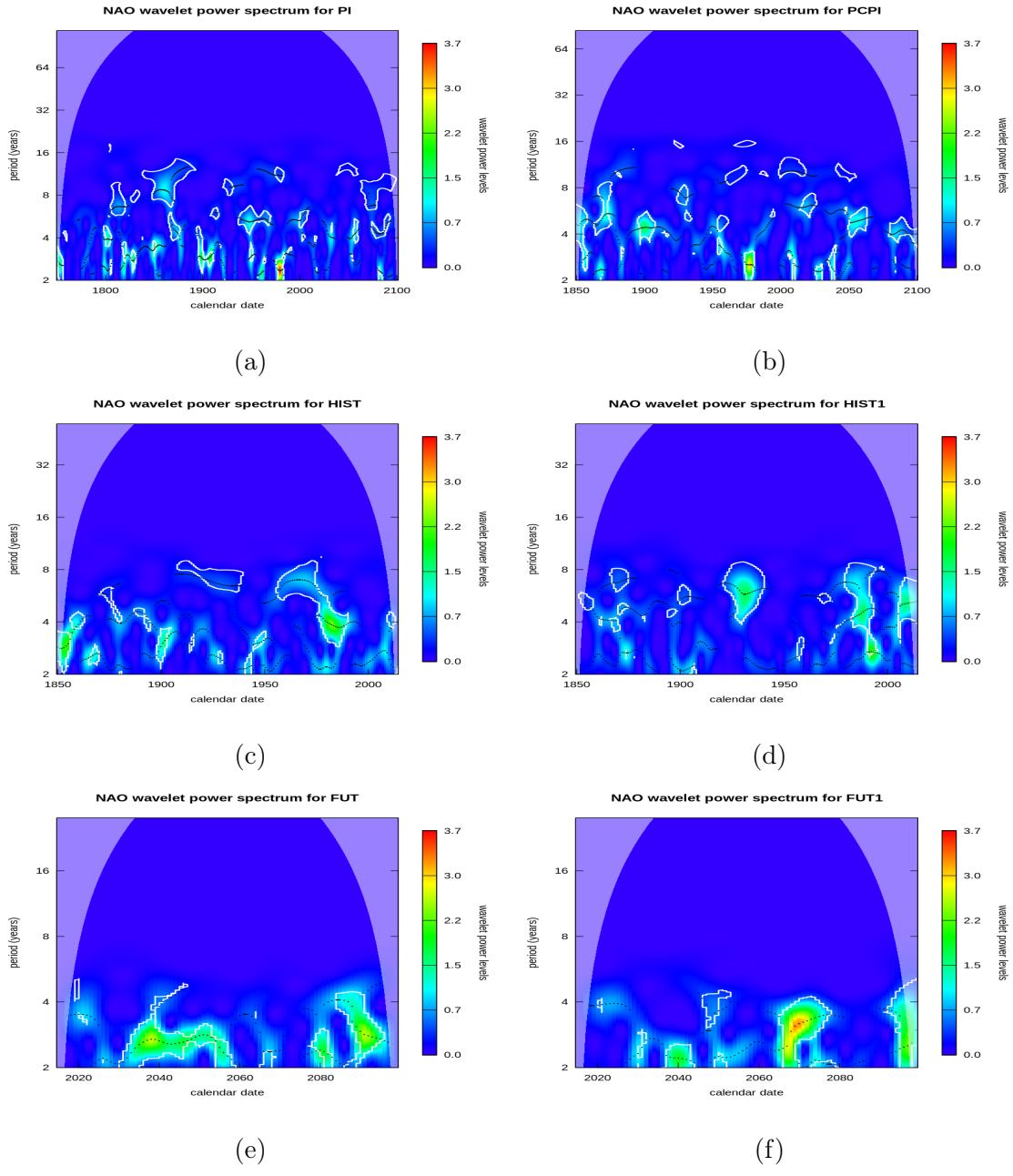

Figure 3.10: (a) The NAO Wavelet power spectrum of the fully coupled preindustrial run (PI). (b) as in (a) but with prescribed windstress of 30 years (PCPI). (c) The NAO Wavelet power spectrum of the fully coupled historical run (HIST). (d) as in (c) but with prescribed windstress of 30 years (HIST1) (e) The NAO Wavelet power spectrum of the fully coupled future Scenario (FUT). (f) as in (e) but for FUT1.

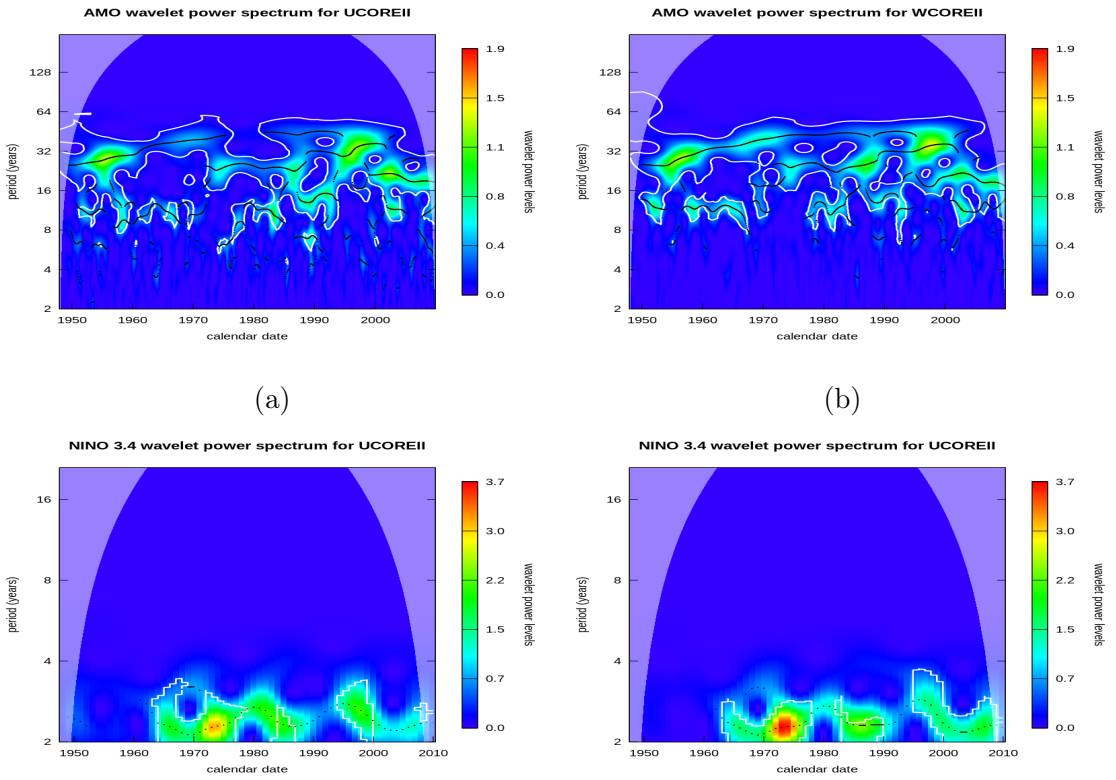

Figure 3.11: (a) The AMO Wavelet power spectrum of the fully coupled historical run (UCOREII). (b) The AMO Wavelet power spectrum of the partially coupled historical run with prescribed windstress of 30 years (WCOREII). (c) The Niño 3.4 Wavelet power spectrum of the fully coupled historical run (UCOREII). (d) The Niño 3.4 Wavelet power spectrum of the partially coupled historical run with prescribed windstress of 30 years (WCOREII).

3.6 Sea Surface Temperature

Sea surface temperature is the temperature of the top of the Ocean's surface. In the fully coupled control run in Fig. 3.12a, there is high temperature just around the equator which is a result of insolation.

There is a massive increase in SST in Amundsen and the Weddell Sea just around the Antarctic by 2°C - 3°C in the PCPI as seen in Fig. 3.12b. This SST increase is also seen in the Scotia Sea, as well as in the Indian Ocean. At the equator, the Gulf of Guinea has a temperature decrease of 2°C, thus highlighting the cooling effect of the prescribed wind stress. The Indian Ocean shows a colossal decrease of 1°C - 2°C in some parts, however with a slight increase in temperature at the south of the Indian Ocean. The North Sea and the Norwegian Sea decrease by 3°C in temperature, while the Greenland and Labrador Seas have a 2°C decrease in SST.

Juxtaposing Fig. 3.12c (HIST) and Fig. 3.12d (HIST1), the HIST1 depicts the increase in SST around the Southern Hemisphere while a decrease in SST is observed in the Northern Hemisphere. Here, the western Pacific ocean decreased by 2°C in Fig. 3.12c (HIST) but increased by the same amount in Fig. 3.12d (HIST1). Across the East, the SST increases gradually for HIST while the reverse is the case for HIST1. There is also an increase in SST in the Labrador sea from HIST to HIST1 but there is a significant decrease in temperature in the Greenland sea. At the equator, there is an increase in SST from West to East in Fig. 3.12e while the opposite is the case for Fig. 3.12f. There is also an increase in SST in the Southern Hemisphere then a slight decrease just around the Antarctic in FUT. while in FUT1 there is a prominent increase in the SH. Up North, there is a decrease of 3°C in the Western and Eastern Pacific Ocean in FUT1 whereas, it remains at maximum for FUT.

However, more cooling effects are observed across the equator from East to West and in the SH towards the Antarctic in the WCOREII in Fig. 3.13b, with Fig. 3.13a as a reference. Prominently, larger parts of the Labrador Sea and the Greenland sea increase by 3 °C in the WCOREII. The intensity of the SST tends to wane in Fig 3.13b.

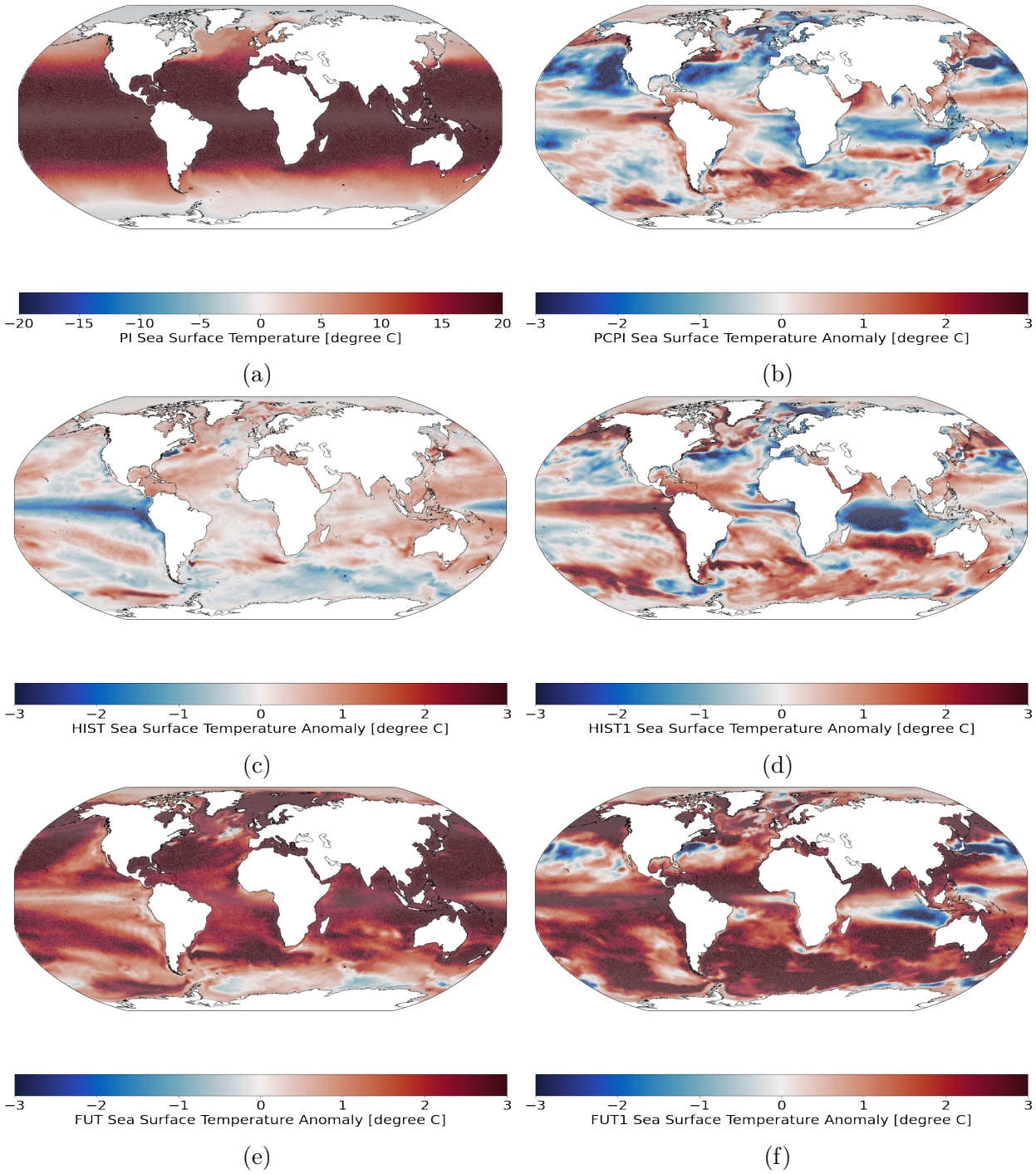

Figure 3.12: Global Sea Surface Temperature of the last 30 years for: (a) the fully coupled control run (2071-2100) and the anomaly for: (b) PCPI (2071-2100) (c) HIST (1985-2014) (d) HIST1 (1985-2014) (e) FUT (2069-2098) (f) FUT1 (2069-2098). The anomalies are computed by subtracting the SST fields in the control run from the SST fields of the individual simulation.

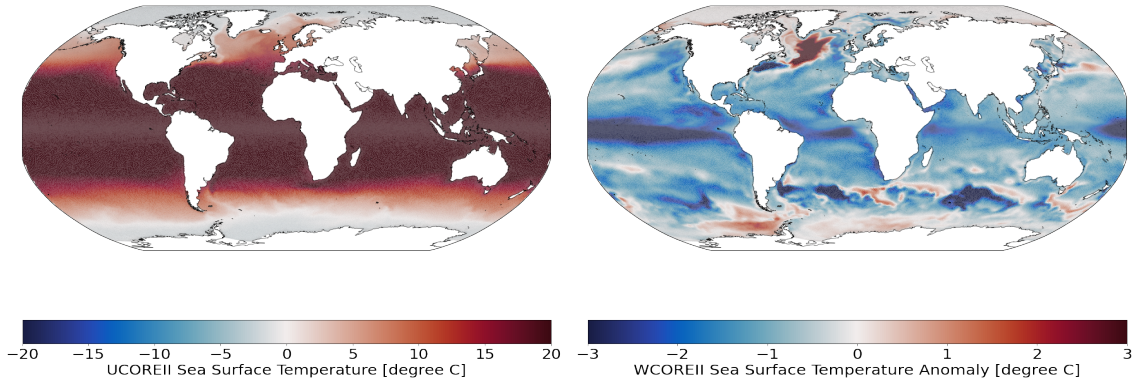

(a) (b)

Figure 3.13: Global Sea Surface Temperature of the last 30 years for the COREII FORCING: (a) UCOREII (1980-2009) and the anomaly for: (b) WCORE (1980-2009). The anomaly here is with respect to the UCOREII.

3.7 Surface Air Temperature

The Surface air temperature (SAT) as seen in Fig. 3.14a highlights the intensity of temperature of the air near the surface of the Earth, measured at 2 meters above the ground or ocean surface. The greatest intensity is observed in the tropical zone which of course suggests the concentration of the sun's radiation due to the sphericity of the earth. The Arctic and Antarctic regions have colder temperatures with the Antarctic having the lowest temperature. The temperatures are low because of the irradiance compared to the lower latitudes invariably accommodating large ice sheets are at the poles due to the low temperatures. The anomaly of the PCPI 3.14b relative to the Fig. 3.14a the PI, indicates the severe SAT decrease in the Seas surrounding Europe, especially the Greenland Sea, Barents Sea, and the Norwegian Sea at about 5°C. Temperature decrease is seen in part of the Indian Ocean extending prominently to the Timor Sea above Australia. While the Amundsen Sea and the Ross Sea around the Antarctic show massive temperature increase to about 4°C. Major Parts of the Western Pacific Ocean show slight increment in temperature, as well as the Scotia Sea around Southern America, increasing in SAT at around 3°C. For the continents, there is temperature decrease in Europe but temperature increase in Antarctica in PCPI. More activities are witnessed in Fig. 3.14d compared to Fig. 3.14c with temperature decrease seen in Greenland to the Barents Sea in the NH to around 5°C. The Timor Sea as well as part of the Eastern Pacific Ocean in the North Mid-latitude zone portrays a temperature decrease of about 3°C - 4°C. Temperature increase is also seen in the Antarctica in HIST1 and in all the continents except Europe and Northern Asia. In Fig. 3.14e, it is evident that there are colossal temperatures gain in all the continents, especially in the Arctic as well as the Antarctic. This observation speaks a large volume of the impact of greenhouse gases. Similar temperatures gain are observed in the Arctic and Antarctic as in Fig. 3.14f, however with some decrease in Greenland and the Barents Sea in the Arctic, the Ross Sea in the Antarctic, the Timor Sea above Australia, and the upper part of the Pacific Ocean. The continents in FUT1 show increase in temperature from FUT. However, the Eurasian continent depicts lower

temperature in FUT1 when compared to FUT.

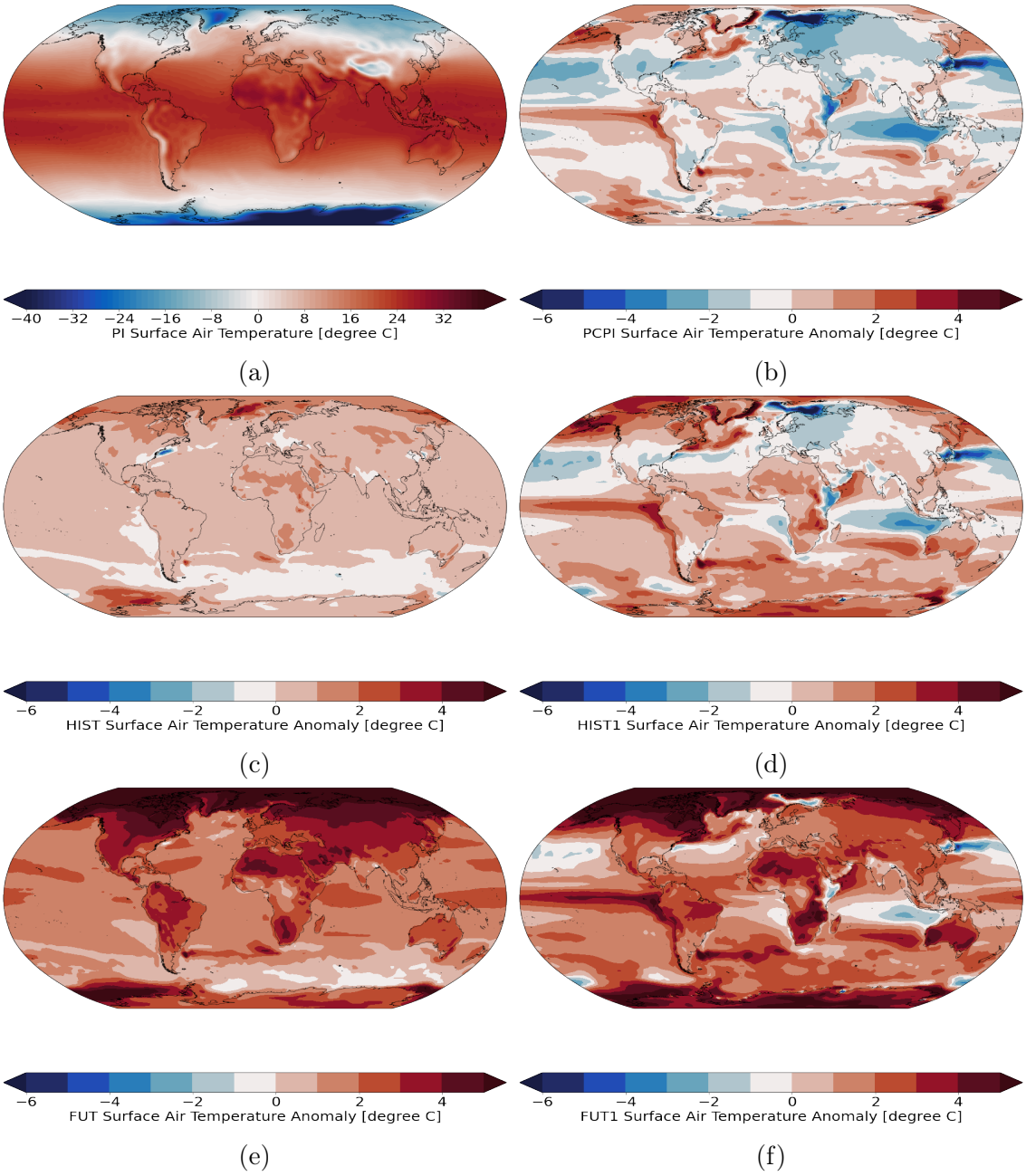

Figure 3.14: Global Sea Surface Temperature of the last 30 years for: (a) the fully coupled control run (2071-2100) and the anomaly for: (b) PCPI (2071-2100) (c) HIST (1985-2014) (d) HIST1 (1985-2014) .The anomalies are computed by subtracting the SST fields in the control run from the SST fields of the individual simulation

Chapter 4

Discussion

The general waning of the intensity of the SST in the partially coupled runs might be suggestive that there is the reduction in the SST by the wind stress as colder subsurface water is brought to the surface. Also, wind stress might lead to rapid evaporation which leads to cooling thus reducing the SST. It is apt to note the negative relationship between SST and wind stress. The Northern Hemisphere close to the Arctic sea-ice boundary, in the Mediterranean, in the Black Sea, and along the northern edge of the Northern Hemisphere western boundary currents show the strongest warming trends as seen in Fig. 3.12c for HIST. Pole-ward warming trends along the southern hemisphere boundary currents reaching the Ross sea are highlighted. In the south of the Gulf Stream in Fig. 3.12c for HIST, the localized cooling trend corresponds to a localized region of increased SST anomaly variability at the edge of the Grand Banks where the cold Labrador Current and warm Gulf Stream meet.(Bulgin et al., 2020).

The cooling in the South Pacific that is evident in the HIST SST has also been observed in several analysis products derived from in-situ observations (Bulgin et al., 2020). Due to the northward advection by Ekman currents of upwelled cold deep-waters, Warming in the South Pacific is expected to be weaker than the global mean Kostov et al.; (2017) and Armour and Bitz; (2000). There however seems to be southward temperature increase in SST for partially coupled runs as seen in Fig. 3.12b, 3.12d, and 3.12f. This could be as a result of the weakening AMOC which is also very prominent in the partially coupled AMOC anomalies in Fig.

3.6 as the weakening of the AMOC will most likely reduce the rate of Northward transfer of warm water, hence the increase in SST in the Southern hemisphere. The atmosphere is unconstrained in the Modini-AWI-ESM. The prescribed wind forcing interacts with the atmosphere only indirectly via the SST response as well as responses of other variables like SLP or humidity to the wind stress. The wind forcing in the partially coupled simulations (Fig. 3.12b, 3.12d, 3.12f) reduces the temperature differences slightly in the Northern Atlantic Ocean and in the Indian Ocean as seen in both the SST and the SAT (Fig. 3.12 and 3.14), thus signifying the relationship between the SST and the SAT. Thoma et al. (2015) suggested that this temperature offset between the fully coupled and partially coupled might be as a result of the 6-hourly wind forced Modini-AWI-ESM which enables more surface mixing and potentially cooler (global mean) SST. Another factor might be the drastic weakening of the AMOC in the partially coupled simulations as mentioned above.

In terms of SAT, the partially coupled runs tend to have a particular trend as though the westerlies are propelled by the prescribed wind forcing thus increasing its impact towards the East, leading to temperature decrease while the cool air temperature is convened by the easterlies back to the West. Some eastern parts also depict a decrease in temperatures which could also be a result of cooling from aerosols. Furthermore, the action center gradients in the partially coupled simulations are higher than that of the fully coupled simulations (Fig. 3.3). This will thereby enhance strong westerlies from the Atlantic towards the Eurasian continent, hence the cooling of the Eurasian continent.

To better investigate the periodicity of the examined variability mechanisms, I performed the wavelet spectral analysis using their corresponding time series. All wavelet spectra displayed their respective quasi-persistent cycles. 50-80years for AMO (Sutton and Hodson, 2005;Knight et al., 2006;Trenberth and Shea, 2006; Dima and Lohmann, 2007,Delworth et al., 2007), 2-7years for ENSO (Kestin et al., 1998;Torrence and Webster, 1999;Schulte et al., 2015), and 2-10years for NAO (Higuchi et al., 1999;Hilmer and Jung, 2000) but interestingly, these cycles are more pronounced in the partially coupled simulations.

The wavelet spectrum gives details on the relative power at a certain scale and a certain time. It portrays the actual oscillations of the individual wavelets, rather than just the magnitude (SANTOS et al., 2001). The 5% significance level in the average wavelet corresponds to the 95% confidence level.

The average wavelet power is used here to show the average power in the bands with high energy and their respective significant peaks. The partially coupled runs are seen to be higher in power, showing more significant peaks when compared with the fully coupled runs. The partially coupled runs as seen in the supplementary figures show maximum frequency response in the average wavelet power spectrum than their fully coupled counterpart.

An El Niño event is characterized by a strong positive temperature anomaly in the equatorial Pacific (Trenberth, 1997). This is in agreement, especially with our partially coupled experiments(Fig. 3.12). It is also in tandem with our Niño 3.4 index time series except for the COREII forcing simulation. Also, the modelled period for the COREII forcing for the AMO is too short to represent the typical 80-year timescale but depicts interannual variation indicating teleconnections with ENSO (Enfield et al., 2001). Howbeit, the COREII forcing of the FESOM standalone gives no information about the AMO and Niño 3.4 as it is constrained by the surface boundary conditions in these indices.

The AMO is well captured by the fully coupled and the partially coupled experiments (Fig. 3.1a, 3.1b, and 3.1c), however, the prominent decrease from the mid-1990s in the historical models (Fig. 3.1b) onward indicate,CO_2 have a significant impact on the AMO. A proper representation of other atmospheric forcings like stratospheric aerosols and ozone, which are also included in CMIP6 experiments, could also have led to the comparable correlation coefficients between fully coupled and Modini-ESM. However, the fully coupled and partially coupled runs are weakly correlated. This negates the significant correlation observed by (Thoma et al., 2015). This could be as a result of the Modini-ESM responding to SST, SLP, and humidity as against only SST for that of Thoma et al. (2015).

The strength and latitudinal position of winds have an important impact on the oceanic heat and the Atlantic Meridional Overturning Circulation (AMOC) thus

affecting the climate Wei et al.; 2012; Toggweiler; 2005 and Speich et al.; 2007. Physically, a northward Ekman transport in the upper layers of the Southern Ocean is induced by enhanced SH winds induce, thereby strengthening the flow of water from the Southern Ocean into the Atlantic. With deep water exiting the Atlantic due to the balance of the Northward flow by the Southern flow at depth, the AMOC is enhanced. Intensified and poleward shifted winds act to enhance the upwelling of North Atlantic Deep Water (NADW) in the Southern Ocean, thereby increasing ocean ventilation (Russell et al., 2006). This intensification of the AMOC is observed in the WCOREII (3.7b) in which the upwelling is greatly enhanced. The nose-diving trend In Fig. 3.5c indicates the presence of greenhouse gases.

The weakening of the AMOC would have major impacts, cooling the North Atlantic and adjacent land regions, e.g., Scandinavia, or reducing the rate of temperature increase associated with global warming (Norel et al., 2021). The weakened AMOC is typically accompanied by slight warming of the Southern Hemisphere (Norel et al., 2021) as in the partially coupled models in 3.12 and 3.14. Future changes in the AMOC could therefore have significant climatic impacts, possibly affecting the North Atlantic sink for CO2, the position of the intertropical convergence zone, the Atlantic storm track, rainfall, and marine ecosystems (Norel et al., 2021). The weakening in the AMOC as seen in this study is in agreement with other studies that show an AMOC weakening for future warming like e.g. Ackermann et al. (2020).

All the AMOC time series well demonstrates conspicuous interannual variability which is a result of wind stress arising primarily from weather noise (Fan and Schneider, 2012) which is unpredictable. The Ocean responded with larger pronounced interannual variability due to the prescribed wind stress as seen in the partially coupled experiments. Implying that a large part of the interannual variability can be a result of wind forcing.

The decadal or interdecadal timescale is related to the surface heat flux Eden and Jung; (2001); and Eden and Willebrand; (2001) prominently seen in the partially coupled runs indicating the role of the wind forcing in heat exchange with the atmosphere. These decadal variations are absent in the COREII forcing experiment

as there is no heat exchange taking place since it is an Ocean, stand-alone model.

To fully capture the spatial configuration of the NAO mode, the need for a non-station-based index is pronounced. To this end quantification of the NAO was achieved by empirical orthogonal function (EOF) analysis of SLP, to generate the spatial modes of the NAO as suggested by Hurrell and Deser (2010). The action center is pronounced in the Icelandic low in the fully coupled runs while it is prominent in the partially coupled runs, howbeit, the NAO of the action center is not in the same position highlighting the non-stationary nature of the NAO as seen in Fig. 3.3. The said action center exhibits a higher gradient in the partially coupled runs.

The NAO response tends to be strengthened when the AMO and Nino 3.4 are in phase as observed in Zhang et al. (2019). This is another indication of the teleconnection that exists among the considered variability. This is however more pronounced in the partially coupled runs due to missing feedback from the ocean to the wind. A weak correlation exists be it for the fully coupled and partially coupled models as seen in the Appendix.

Chapter 5

Summary and Conclusions

The main aim of this paper is not to give an in-depth analysis of the examined variability but to compare the Ocean's effect to the wind stress engendered changes in the partially coupled model with the fully coupled model.

The influence of wind stress forcing on the Ocean has been simulated, analyzing the direct response of the Ocean and the indirect response of the atmosphere using a fully coupled and a partially coupled model in the North Atlantic region. The Ocean has a negative feedback response to wind stress.

The fully coupled AWI-ESM was extended by assimilating the prescribed wind stress in forcing the oceanic component (FESOM) as implemented by Thoma et al. (2015). This is an easy-to-implement method because the Ocean models already provide options for external wind forcing. This method interferes with the ESM only through the two-dimensional wind stress at the Ocean's surface, while all other feedback exists as in the fully coupled AWI-ESM. I have examined the Ocean's response to these prescribed wind stress by reproducing parts of the climate variability of several major modes (e.g. ENSO, NAO, AMO) as well as the response of the SST and SAT. Even the Meridional Overturning circulation.

The partially coupled model, therefore, enables the examining of the effect of wind stress on the Ocean with this study highlighting that the prescribed wind stress enabled experiments to portray the weakening of the AMOC.

The EOF analysis which is impacted by the movement of the action centers has been very distinguished in the partially coupled runs as the magnitude of the action

center diminishes completely in the low-pressure action center while it enlarges in the high-pressure action center. In response to the wind stress, the magnitude of the high-pressure action center prevails over the drifting of the action center. The high gradient action center in the partially coupled simulations would enable mild westerlies from the Atlantic to the Eurasian continent. This further impacts the SAT, causing cooling in the Eurasian continent.

There generally seems to be a shift in SST as the Antarctic appears to heat up more than the Arctic in the partially coupled models. This is a result of the drastic weakening AMOC in the partially coupled simulations.

In general, the partially coupled models have shown negative feedback to the wind stress in respect to the fully coupled models in examined indices. It has been shown that there is a clear link between the wind forcing and Northward Ocean heat transport causing cooling with the reversed heat transported to Southward Ocean heating it up which might increase the rate of melting and depletion of ice sheets in the Antarctic.

In the experiment, the impact of the wind stress-induced Ocean changes how the atmosphere can be assessed. The Surface air temperatures are substantially lower over the high latitudes in the Northern Hemisphere and somewhat higher in the Southern Hemisphere.

Also, it should be noted that the part of the feedback effect is suppressed by the partial coupling. While the atmospheric model component responds to the oceanic changes, the Ocean model component does not receive information of the response in the wind field for the sake of clarity of the experiment its wind forcing is prescribed and the air–ocean momentum forcing is decoupled (Kovács et al., 2020).

Chapter 6

Limitations and Outlook

The configuration of the model enabled us to compare and contrast the fully coupled and partially coupled models with regards to the Ocean's response as well as the atmospheric response though, indirectly. But it is important we compare the observed data set with our models as the standalone models are not sufficient in simulating anything related to surface boundary conditions.

The NAO can be further investigated in terms of phase periods (Negative and Positive) in order to investigate the drift in the high- and low-pressure action center. For the atmospheric evaluation, the advective heat transport can also be considered.

Acronyms

AMO Atlantic Multidecadal Oscillation.

AMOC Atlantic Meridional Overturning Circulation.

AWI Alfred Wegener Institute.

ECHAM European Center-Hamburg Model.

ECHAM6 European Center-Hamburg Model, Version 6.

ENSO El Niño-Southern Oscillation.

EOF Empirical Orthogonal Function.

FESOM Finite Element Sea-ice Ocean Circulation Model.

FUT fully coupled future scenario run.

FUT1 Partially coupled future scenario run.

HIST Fully Coupled Historical run.

HIST1 Partially coupled historical run.

NAO North Atlantic Oscillation.

NH Northern Hemisphere.

PCPI Partially coupled Pre-Industral run.

SH Southern Hemisphere.

SLP Sea Level Pressure.

SST Sea Surface Temperature.

UCOREII unperturbed COREII run.

WCOREII perturbed COREII run.

Appendix A

SUPPLEMENTARY

Table A.1: Pearson Correlation for the fully coupled vs the partially coupled model.

Name of Experiments	**correlation**	**Significance**
HIST vs HIST1 (AMO)	0.03	nil
FUT vs FUT1 (AMO)	0.06	weak
HIST vs HIST1 (NINO 3.4)	-0.12	Weak
FUT vs FUT1 (NINO 3.4)	-0.01	nil
HIST vs HIST1 (NAO)	0.04	nil
FUT vs FUT1 (NAO)	0.09	Weak
UCOREII vs WCOREII (AMO)	0.68	High
UCOREII vs WCOREII (NINO 3.4)	0.96	High

Table A.2: Pearson Correlation for AMO vs NINO 3.4 with the AWI-ESM.

Name of Experiments	**correlation**	**Significance**
PCPI	0.41	Weak
HIST	0.27	Weak
HIST1	0.34	Weak
FUT	0.41	weak
FUT1	0.36	weak
UCOREII	0.14	Weak
WCOREII	0.31	Weak

Table A.3: Pearson Correlation for AMO vs NAO with the AWI-ESM.

Name of Experiments	**correlation**	**Significance**
PCPI	0.23	Weak
HIST	0.13	Weak
HIST1	0.14	Weak
FUT	0.15	Weak
FUT1	0.13	Weak

Table A.4: Pearson Correlation for NINO 3.4 vs NAO with the AWI-ESM.

Name of Experiments	**correlation**	**Significance**
PCPI	0.17	Weak
HIST	0.15	Weak
HIST1	0.04	nil
FUT	0.009	nil
FUT1	0.08	Weak

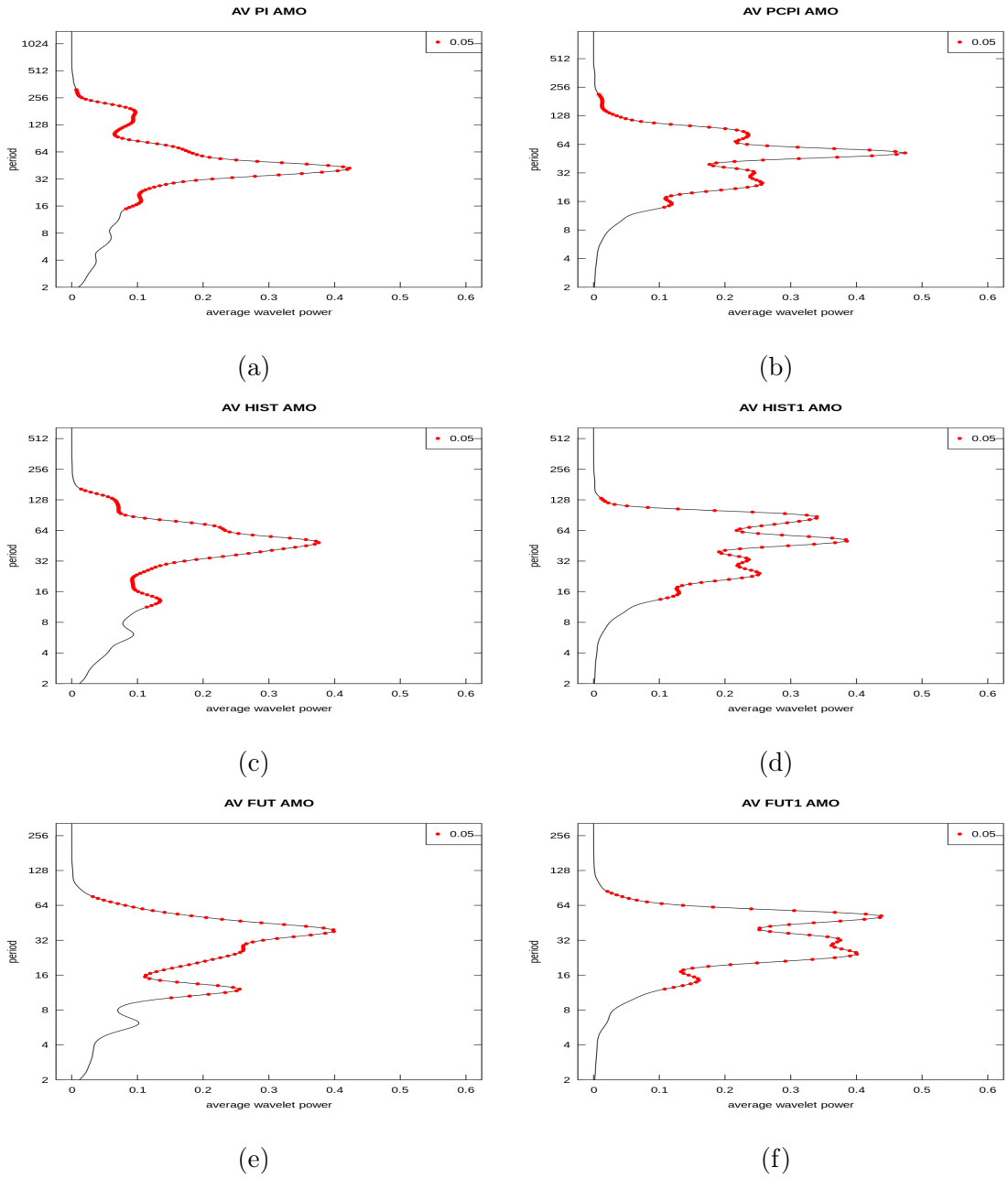

Figure A.1: The AMO average wavelet spectrum for the: (a) fully coupled pre-industrial run (PI). (b) PCPI . (c) HIST. (d) HIST1. (e) FUT and (f) FUT1

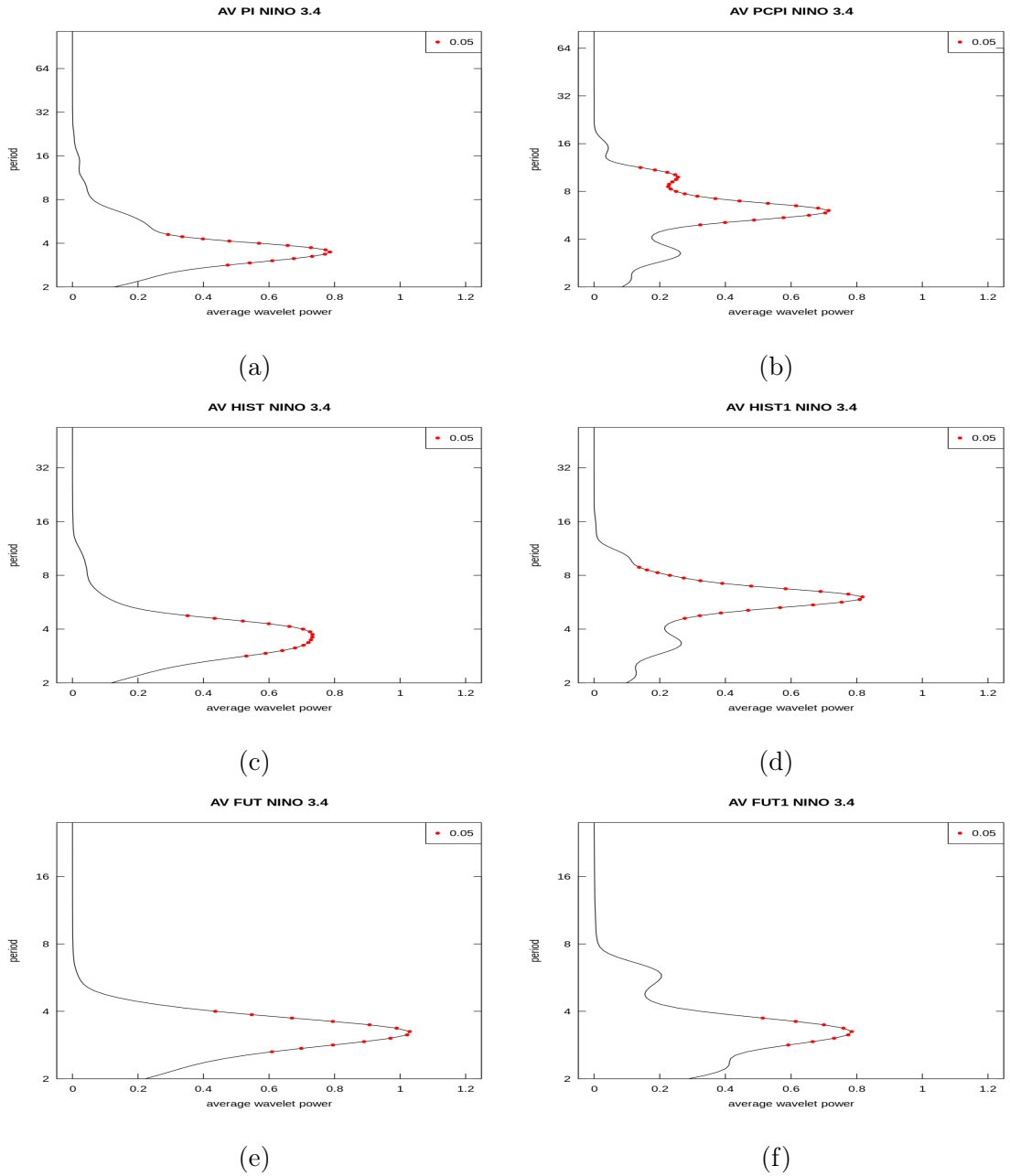

Figure A.2: The NINO 3.4 average wavelet spectrum for the: (a) fully coupled pre-industrial run (PI). (b) PCPI . (c) HIST. (d) HIST1. (e) FUT and (f) FUT1

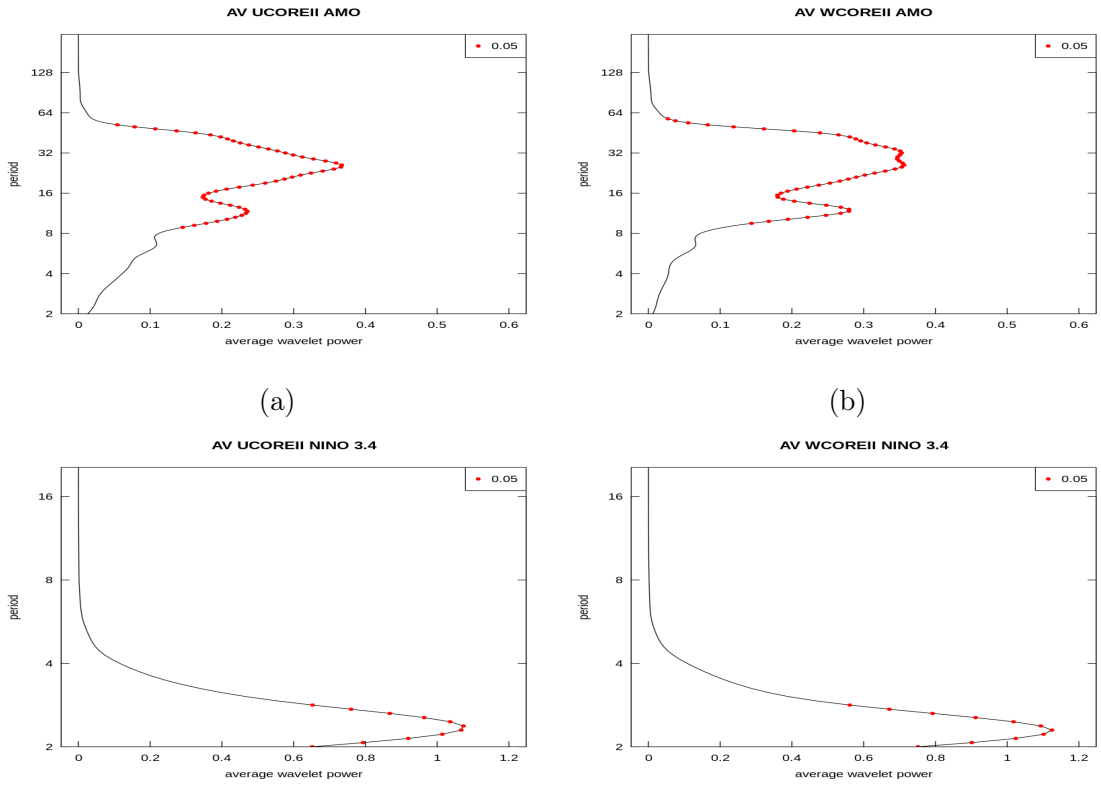

Figure A.3: (a) The AMO average wavelet power for UCOREII. (b) as in (a) but for WCOREII. (c) The Nino 3.4 average wavelet power for UCOREII and (d) as in (c) but for WCOREII.

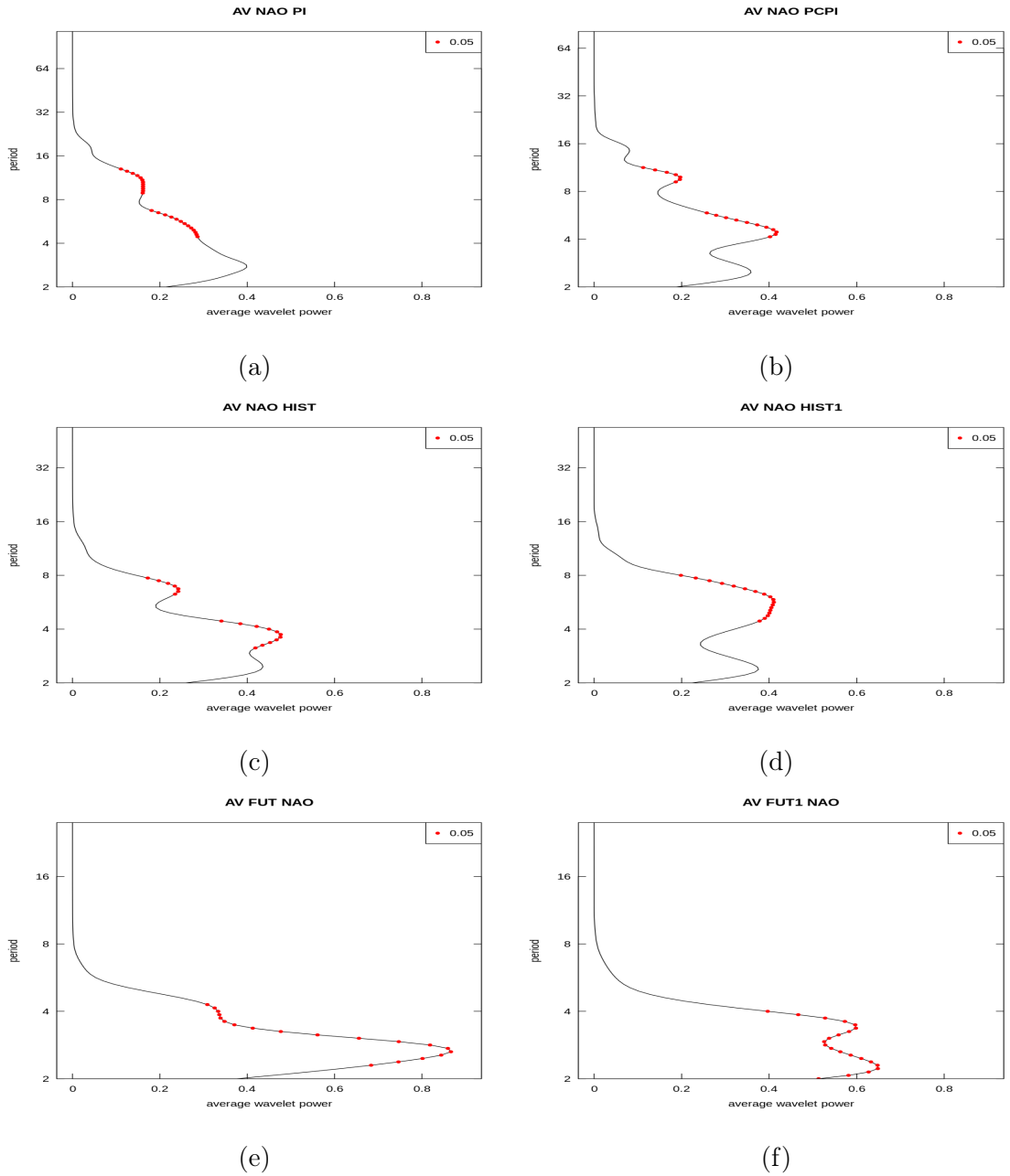

Figure A.4: The NAO average wavelet spectrum for the: (a) fully coupled pre-industrial run (PI). (b) PCPI . (c) HIST. (d) HIST1. (e) FUT and (f) FUT1

Bibliography

Ackermann, L., Danek, C., Gierz, P., and Lohmann, G. (2020). Amoc recovery in a multicentennial scenario using a coupled atmosphere-ocean-ice sheet model. *Geophysical Research Letters*, 47(16):e2019GL086810.

Armour, K. C. and Bitz, C. M. (2000). Observed and projected trends in antarctic sea ice. *US CLIVAR*, 500:12.

Bjerknes, J. (1964). Atlantic air-sea interaction. In *Advances in geophysics*, volume 10, pages 1–82. Elsevier.

Brown, J. R., Brierley, C. M., An, S.-I., Guarino, M.-V., Stevenson, S., Williams, C. J., Zhang, Q., Zhao, A., Abe-Ouchi, A., Braconnot, P., et al. (2020). Comparison of past and future simulations of enso in cmip5/pmip3 and cmip6/pmip4 models. *Climate of the Past*, 16(5):1777–1805.

Bulgin, C. E., Merchant, C. J., and Ferreira, D. (2020). Tendencies, variability and persistence of sea surface temperature anomalies. *Scientific reports*, 10(1):1–13.

Cayan, D. R. (1992). Latent and sensible heat flux anomalies over the northern oceans: The connection to monthly atmospheric circulation. *Journal of climate*, 5(4):354–369.

Danabasoglu, G., Yeager, S. G., Bailey, D., Behrens, E., Bentsen, M., Bi, D., Biastoch, A., Böning, C., Bozec, A., Canuto, V. M., et al. (2014). North atlantic simulations in coordinated ocean-ice reference experiments phase ii (core-ii). part i: mean states. *Ocean Modelling*, 73:76–107.

Danek, C., Scholz, P., and Lohmann, G. (2019). Effects of high resolution and spinup time on modeled north atlantic circulation. *Journal of Physical Oceanography*, 49(5):1159–1181.

Danilov, S., Kivman, G., and Schröter, J. (2004). A finite-element ocean model: principles and evaluation. *Ocean Modelling*, 6(2):125–150.

Danilov, S., Sidorenko, D., Wang, Q., and Jung, T. (2017). The finite-volume sea ice–ocean model (fesom2). *Geoscientific Model Development*, 10(2):765–789.

Dee, D. P., Uppala, S. M., Simmons, A., Berrisford, P., Poli, P., Kobayashi, S., Andrae, U., Balmaseda, M., Balsamo, G., Bauer, d. P., et al. (2011). The era-interim reanalysis: Configuration and performance of the data assimilation system. *Quarterly Journal of the royal meteorological society*, 137(656):553–597.

Delworth, T. L., Zhang, R., and Mann, M. E. (2007). Decadal to centennial variability of the atlantic from observations and models. *Geophysical Monograph-American Geophysical Union*, 173:131.

Dima, M. and Lohmann, G. (2007). A hemispheric mechanism for the atlantic multidecadal oscillation. *Journal of Climate*, 20(11):2706–2719.

Ding, H., Greatbatch, R. J., Latif, M., Park, W., and Gerdes, R. (2013). Hindcast of the 1976/77 and 1998/99 climate shifts in the pacific. *Journal of Climate*, 26(19):7650–7661.

Eden, C. and Jung, T. (2001). North atlantic interdecadal variability: oceanic response to the north atlantic oscillation (1865–1997). *Journal of Climate*, 14(5):676–691.

Eden, C. and Willebrand, J. (2001). Mechanism of interannual to decadal variability of the north atlantic circulation. *Journal of Climate*, 14(10):2266–2280.

Enfield, D. B., Mestas-Nuñez, A. M., and Trimble, P. J. (2001). The atlantic multidecadal oscillation and its relation to rainfall and river flows in the continental us. *Geophysical Research Letters*, 28(10):2077–2080.

Fan, M. and Schneider, E. K. (2012). Observed decadal north atlantic tripole sst variability. part i: Weather noise forcing and coupled response. *Journal of the Atmospheric Sciences*, 69(1):35–50.

Hanna, E., Cropper, T. E., Jones, P. D., Scaife, A. A., and Allan, R. (2015). Recent seasonal asymmetric changes in the nao (a marked summer decline and increased winter variability) and associated changes in the ao and greenland blocking index. *International Journal of Climatology*, 35(9):2540–2554.

He, Y.-C., Drange, H., Gao, Y., and Bentsen, M. (2016). Simulated atlantic meridional overturning circulation in the 20th century with an ocean model forced by reanalysis-based atmospheric data sets. *Ocean Modelling*, 100:31–48.

Higuchi, K., Huang, J., and Shabbar, A. (1999). A wavelet characterization of the north atlantic oscillation variation and its relationship to the north atlantic sea surface temperature. *International Journal of Climatology: A Journal of the Royal Meteorological Society*, 19(10):1119–1129.

Hilmer, M. and Jung, T. (2000). Evidence for a recent change in the link between the north atlantic oscillation and arctic sea ice export. *Geophysical Research Letters*, 27(7):989–992.

Hurrell, J. and Dickson, R. (2004). Climate variability over the north atlantic. marine ecosystems and climate variation/stenseth nc, ottersen g., hurrell jw, and belgrango a. marine ecosystems and climate variation. the north atlantic: a comparative perspective.

Hurrell, J. W. (1995). Decadal trends in the north atlantic oscillation: Regional temperatures and precipitation. *Science*, 269(5224):676–679.

Hurrell, J. W. and Deser, C. (2010). North atlantic climate variability: the role of the north atlantic oscillation. *Journal of marine systems*, 79(3-4):231–244.

Iacono, M. J., Delamere, J. S., Mlawer, E. J., Shephard, M. W., Clough, S. A., and Collins, W. D. (2008). Radiative forcing by long-lived greenhouse gases: Calculations with the aer radiative transfer models. *Journal of Geophysical Research: Atmospheres*, 113(D13).

Karspeck, A., Stammer, D., Köhl, A., Danabasoglu, G., Balmaseda, M., Smith, D., Fujii, Y., Zhang, S., Giese, B., Tsujino, H., et al. (2017). Comparison of the atlantic meridional overturning circulation between 1960 and 2007 in six ocean reanalysis products. *Climate Dynamics*, 49(3):957–982.

Kestin, T. S., Karoly, D. J., Yano, J.-I., and Rayner, N. A. (1998). Time–frequency variability of enso and stochastic simulations. *Journal of Climate*, 11(9):2258–2272.

Knight, J. R., Folland, C. K., and Scaife, A. A. (2006). Climate impacts of the atlantic multidecadal oscillation. *Geophysical Research Letters*, 33(17).

Kostov, Y., Marshall, J., Hausmann, U., Armour, K. C., Ferreira, D., and Holland, M. M. (2017). Fast and slow responses of southern ocean sea surface temperature to sam in coupled climate models. *Climate Dynamics*, 48(5-6):1595–1609.

Kovács, T., Gerdes, R., and Marshall, J. (2020). Wind feedback mediated by sea ice in the nordic seas. *Journal of Climate*, 33(15):6621–6632.

Large, W. and Yeager, S. (2009). The global climatology of an interannually varying air–sea flux data set. *Climate dynamics*, 33(2-3):341–364.

Li, J. and Titi, E. S. (2019). The primitive equations as the small aspect ratio limit of the navier–stokes equations: Rigorous justification of the hydrostatic approximation. *Journal de Mathématiques Pures et Appliquées*, 124:30–58.

Lim, Y.-K., Schubert, S. D., Kovach, R., Molod, A. M., and Pawson, S. (2018). The roles of climate change and climate variability in the 2017 atlantic hurricane season. *Scientific reports*, 8(1):1–10.

Lohmann, G., Butzin, M., Eissner, N., Shi, X., and Stepanek, C. (2020). Abrupt climate and weather changes across time scales. *Paleoceanography and Paleoclimatology*, 35(9):e2019PA003782.

Lohmann, K., Drange, H., and Bentsen, M. (2009). Response of the north atlantic subpolar gyre to persistent north atlantic oscillation like forcing. *Climate dynamics*, 32(2-3):273–285.

Loveland, T. R., Reed, B. C., Brown, J. F., Ohlen, D. O., Zhu, Z., Yang, L., and Merchant, J. W. (2000). Development of a global land cover characteristics database and igbp discover from 1 km avhrr data. *International Journal of Remote Sensing*, 21(6-7):1303–1330.

Mantua, N. J., Hare, S. R., Zhang, Y., Wallace, J. M., and Francis, R. C. (1997). A pacific interdecadal climate oscillation with impacts on salmon production. *Bulletin of the american Meteorological Society*, 78(6):1069–1080.

Norel, M., Kałczyński, M., Pińskwar, I., Krawiec, K., and Kundzewicz, Z. W. (2021). Climate variability indices—a guided tour. *Geosciences*, 11(3):128.

Okumura, Y., Xie, S.-P., Numaguti, A., and Tanimoto, Y. (2001). Tropical atlantic air-sea interaction and its influence on the nao. *Geophysical Research Letters*, 28(8):1507–1510.

Raddatz, T., Reick, C., Knorr, W., Kattge, J., Roeckner, E., Schnur, R., Schnitzler, K.-G., Wetzel, P., and Jungclaus, J. (2007). Will the tropical land biosphere dominate the climate–carbon cycle feedback during the twenty-first century? *Climate dynamics*, 29(6):565–574.

Roeckner, E., Brokopf, R., Esch, M., Giorgetta, M., Hagemann, S., Kornblueh, L., Manzini, E., Schlese, U., and Schulzweida, U. (2006). Sensitivity of simulated climate to horizontal and vertical resolution in the echam5 atmosphere model. *Journal of Climate*, 19(16):3771–3791.

Russell, J. L., Dixon, K. W., Gnanadesikan, A., Stouffer, R. J., and Toggweiler, J. (2006). The southern hemisphere westerlies in a warming world: Propping open the door to the deep ocean. *Journal of Climate*, 19(24):6382–6390.

Saha, S., Moorthi, S., Pan, H.-L., Wu, X., Wang, J., Nadiga, S., Tripp, P., Kistler, R., Woollen, J., Behringer, D., et al. (2010). The ncep climate forecast system reanalysis. *Bulletin of the American Meteorological Society*, 91(8):1015–1058.

SANTOS, C. A., GALVÃO, C. d. O., SUZUKI, K., and TRIGO, R. M. (2001). Matsuyama city rainfall data analysis using wavelet transform. *Proceedings of Hydraulic Engineering*, 45:211–216.

Scholz, P., Lohmann, G., Wang, Q., and Danilov, S. (2013). Evaluation of a finite-element sea-ice ocean model (fesom) set-up to study the interannual to decadal variability in the deep-water formation rates. *Ocean Dynamics*, 63(4):347–370.

Schulte, J., Duffy, C., and Najjar, R. (2015). Geometric and topological approaches to significance testing in wavelet analysis. *Nonlinear Processes in Geophysics*, 22(2):139–156.

Servonnat, J., Mignot, J., Guilyardi, E., Swingedouw, D., Séférian, R., and Labetoulle, S. (2015). Reconstructing the subsurface ocean decadal variability using surface nudging in a perfect model framework. *Climate dynamics*, 44(1-2):315–338.

Shi, X. and Lohmann, G. (2016). Simulated response of the mid-holocene atlantic meridional overturning circulation in echam6-fesom/mpiom. *Journal of Geophysical Research: Oceans*, 121(8):6444–6469.

Shi, X., Lohmann, G., Sidorenko, D., and Yang, H. (2020). Early-holocene simulations using different forcings and resolutions in awi-esm. *The Holocene*, 30(7):996–1015.

Sidorenko, D., Goessling, H., Koldunov, N., Scholz, P., Danilov, S., Barbi, D., Cabos, W., Gurses, O., Harig, S., Hinrichs, C., et al. (2019). Evaluation of fesom2. 0 coupled to echam6. 3: preindustrial and highresmip simulations. *Journal of Advances in Modeling Earth Systems*, 11(11):3794–3815.

Sidorenko, D., Rackow, T., Jung, T., Semmler, T., Barbi, D., Danilov, S., Dethloff, K., Dorn, W., Fieg, K., Gößling, H. F., et al. (2015). Towards multi-resolution global climate modeling with echam6–fesom. part i: model formulation and mean climate. *Climate Dynamics*, 44(3-4):757–780.

Sidorenko, D., Wang, Q., Danilov, S., and Schröter, J. (2011). Fesom under coordinated ocean-ice reference experiment forcing. *Ocean Dynamics*, 61(7):881–890.

Small, R. d., deSzoeke, S. P., Xie, S., O'neill, L., Seo, H., Song, Q., Cornillon, P., Spall, M., and Minobe, S. (2008). Air–sea interaction over ocean fronts and eddies. *Dynamics of Atmospheres and Oceans*, 45(3-4):274–319.

Speich, S., Blanke, B., and Cai, W. (2007). Atlantic meridional overturning circulation and the southern hemisphere supergyre. *Geophysical Research Letters*, 34(23).

Steele, M., Morley, R., and Ermold, W. (2001). Phc: A global ocean hydrography with a high-quality arctic ocean. *Journal of Climate*, 14(9):2079–2087.

Stevens, B., Giorgetta, M., Esch, M., Mauritsen, T., Crueger, T., Rast, S., Salzmann, M., Schmidt, H., Bader, J., Block, K., et al. (2013). Atmospheric component of the mpi-m earth system model: Echam6. *Journal of Advances in Modeling Earth Systems*, 5(2):146–172.

Sutton, R. T. and Hodson, D. L. (2005). Atlantic ocean forcing of north american and european summer climate. *science*, 309(5731):115–118.

Thoma, M., Gerdes, R., Greatbatch, R. J., and Ding, H. (2015). Partially coupled spin-up of the mpi-esm: implementation and first results. *Geoscientific Model Development*, 8(1):51–68.

Toggweiler, J. (2005). The mid-latitude westerlies, atmospheric co2, and climate change during the ice ages. In *AGU Spring Meeting Abstracts*, volume 2005, pages OS13A–03.

Torrence, C. and Webster, P. J. (1999). Interdecadal changes in the enso–monsoon system. *Journal of climate*, 12(8):2679–2690.

Trenberth, K. E. (1997). The definition of el nino. *Bulletin of the American Meteorological Society*, 78(12):2771–2778.

Trenberth, K. E. and Shea, D. J. (2006). Atlantic hurricanes and natural variability in 2005. *Geophysical research letters*, 33(12).

Vecchi, G. A., Xie, S.-P., and Fischer, A. S. (2004). Ocean–atmosphere covariability in the western arabian sea. *Journal of climate*, 17(6):1213–1224.

Wang, X., Wang, Q., Sidorenko, D., Danilov, S., Schröter, J., and Jung, T. (2012). Long-term ocean simulations in fesom: evaluation and application in studying the impact of greenland ice sheet melting. *Ocean Dynamics*, 62(10-12):1471–1486.

Wei, W., Lohmann, G., and Dima, M. (2012). Distinct modes of internal variability in the global meridional overturning circulation associated with the southern hemisphere westerly winds. *Journal of Physical Oceanography*, 42(5):785–801.

Xie, S.-P. (2004). Satellite observations of cool ocean–atmosphere interaction. *Bulletin of the American Meteorological Society*, 85(2):195–208.

Zhang, W., Mei, X., Geng, X., Turner, A. G., and Jin, F.-F. (2019). A nonstationary enso–nao relationship due to amo modulation. *Journal of Climate*, 32(1):33–43.